Journal of Controlled Release 382 (2025) 113669

Contents lists available at ScienceDirect

Journal of Controlled Release

journal homepage: www.elsevier.com/locate/jconrel

# Bone marrow vessels are hyperpermeable to macromolecules and nanoscale medicine in a size-dependent manner

John D. Martin [a], Kazuko Toh [b], Margaret R. Martin [a], Pengwen Chen [a], Chenyu Wang [c], Kazunori Igarashi [a], Fotios Mpekris [d], Triantafyllos Stylianopoulos [d], Matthew D. Stuber [c,*], Kazunori Kataoka [b,*], Horacio Cabral [a,*]

[a] *Department of Bioengineering, Graduate School of Engineering, The University of Tokyo, Bunkyo, Tokyo, Japan*
[b] *Innovation Center of NanoMedicine, Kawasaki Institute of Industrial Promotion, Kawasaki, Kanagawa, Japan*
[c] *Process Systems and Operations Research Laboratory, Department of Chemical and Biomolecular Engineering, University of Connecticut, Storrs, CT, USA*
[d] *Cancer Biophysics Laboratory, Department of Mechanical and Manufacturing Engineering, University of Cyprus, Nicosia, Cyprus*

## ARTICLE INFO

*Keywords:*
Nanocarrier
Bone marrow
Intravital microscopy
Transvascular transport

## ABSTRACT

Bone marrow (BM) has roles in health and disease, so systemically administered nanocarriers (NCs) targeting or avoiding BM are desirable. While the hydrodynamic diameter of NCs can be tuned to target or avoid various organs, the size dependence of extravasation from BM vessels is unknown. To clarify the size dependence of passive transvascular transport in the BM, we performed vessel permeability measurements in murine calvaria using confocal fluorescent microscopy with fluorescently labeled dextrans, albumin, and polymeric micelles as model probes. Unexpectedly, we found the permeability of BM vessels to macromolecules decreases with increasing hydrodynamic diameter between 4 nm and 32 nm. We modeled this permeability data with mathematical models to predict an effective pore size for sinusoids of 47 nm and non-sinusoids of 37 nm, with estimated maximum pore sizes of 61 nm and 53 nm, respectively. Finally, we tested these model predictions by demonstrating that the extravasation of 70 nm polymeric micelles, which are larger than the estimated maximum pore size, is hindered relative to 30 nm polymeric micelles. These results establish design criteria for controlling NC hydrodynamic diameter towards modulating delivery to BM.

## 1. Introduction

Bone marrow (BM) generates and stores progenitor cells that enter the circulation and control oxygen transport and immune functions including defense against wounds and pathogens [1]. Given the importance of this organ, researchers aim to develop nanocarriers (NCs) that either avoid delivering toxic anti-cancer drugs to the bone marrow [2,3] or target bone marrow cells by screening libraries of nanoparticles [4]. Regulating BM cells and their transport [5], as well as the delivery of NCs, are small blood vessels known as sinusoids, which lack a continuous basement membrane. They are located in the BM adjacent to non-dividing stem cells [6] and permit passage of BM cells into the circulation through transient fenestrations [7–9]. These holes in the basement membrane and endothelial cells enable transvascular transport of BM cells, but are also present in tumor vessels, which, unlike most normal blood vessels, are hyperpermeable to proteins, antibodies, and NCs with hydrodynamic diameters up to 100 nm and larger [10]. Nonetheless, whether BM sinusoids are hyperpermeable to nanoscale medicine is unclear.

Until recently, BM sinusoids were believed to have a physiologic upper pore limit of 5 nm to transvascular flow when not mediating cellular transport [11], even though *ex vivo* electron microscopy studies revealed that BM sinusoids had 20 nm gaps between endothelial cells and lacked tight, membrane-to-membrane intercellular junctions [12]. Such an assumption is based on several studies reporting that NCs larger than 5 nm in hydrodynamic diameter did not pass through the BM vessel wall except through endocytosis by endothelial cells [13–17]. Recently, researchers demonstrated BM sinusoids and non-sinusoids are hyperpermeable to macromolecules larger than 5 nm by measuring high transvascular transport rates (*i.e.*, effective permeability) of bovine

---

This article is part of a Special issue entitled: 'ESCDD2022' published in Journal of Controlled Release.

* Corresponding authors.

*E-mail addresses:* stuber@alum.mit.edu (M.D. Stuber), kkataoka@g.ecc.u-tokyo.ac.jp (K. Kataoka), horacio@bmw.t.u-tokyo.ac.jp (H. Cabral).

https://doi.org/10.1016/j.jconrel.2025.113669
Received 30 June 2024; Received in revised form 22 January 2025; Accepted 27 March 2025

serum albumin [18,19] (BSA, ~8 nm hydrodynamic diameter [20]) and 70 kDa dextrans [5,21] (~13 nm hydrodynamic diameter [20]). Thus, there is a need to clarify the size dependence of NC hydrodynamic diameter on BM vessel permeability.

BM vessels are hyperpermeable to dextrans up to 13 nm in hydrodynamic diameter, but to what extent this physicochemical parameter of the NC matters is unclear. Uncovering the size-dependence of bone marrow vessels to NC permeability could provide another design parameter of NCs to tune for pharmacokinetics. In this study, we use dextrans as a model NC to show that BM vessel permeability is dependent on size between 4 nm and 13 nm, as well as between 13 nm and 32 nm. Also, BM vessel permeability depends on macromolecule stiffness. Using this intravital permeability data, we use mathematical models to estimate the functional vessel wall pore sizes of BM vessels and the theoretical maximum pore sizes. Finally, we confirm these model predictions by comparing the extravasation of polymeric micelles on either side of the pore cutoff sizes. Thus, we found that the transport of macromolecules and nanoscale medicine from the vasculature into the bone marrow is sensitive to size.

## 2. Methods

### 2.1. Materials

*N,N*-Dimethylformamide (DMF) and dimethyl sulfoxide (DMSO) were purchased from Wako Pure Chemical Co., Inc. (Osaka, Japan). α-Methoxy-ω-aminopoly(ethylene glycol) ($CH_3O$-PEG-$NH_2$; MW = 12,000) was obtained from NOF Co., Inc. (Tokyo, Japan). Fluorescently-labeled dextrans (RITC-70 kDa, FITC-10 kDA, FITC-500 kDa and FITC-2000 kDa), fluorescently labeled bovine serum albumin (FITC-BSA), and γ-Benzyl-L-glutamate and $AgNO_3$ were purchased from Sigma Chemical Co., Inc. (St. Louis, MO). Bis(trichloromethyl) carbonate (triphosgene) was obtained from Tokyo Kasei Kogyo Co., Inc. (Tokyo, Japan). Dichloro (1,2-diaminocyclohexane)platinum(II) (DACHPt$Cl_2$) was purchased from Heraeus (Germany). Alexa 488- and Alexa 647-succinimidyl esters were purchased from Thermo Fisher (Waltham, Massachusetts, United States). The physical properties of the dextrans and BSA are contained in Supplementary Information Table S6.

### 2.2. Mouse models

Immunocompetent BALB/c mice (6-week-old, female) were used for all studies. All animal experiments were approved and performed in accordance with the Guidelines for the Care and Use of Laboratory Animals as stated by The University of Tokyo and the Innovation Center of NanoMedicine (Kawasaki, Japan).

### 2.3. Preparation of (1,2-diaminocyclohexane)platinum(II) (DACHPt)-loaded micelles with 30- and 70-nm

Fluorescent-labeled DACHPt-loaded micelles (DACHPt/m) with sizes of 30 nm and 70 nm were synthesized using our previously established method [22]. For making 30-nm DACHPt/m, we used Alexa488-labeled poly(ethylene glycol)-poly(glutamic acid) (PEG-P(Glu)) block copolymers. For making 70-nm DACHPt/m, we used Alexa647-labeled PEG-P(Glu) block copolymers. The size distribution of DACHPt/m was confirmed by dynamic light scattering DLS measurement at 25 °C using a Zetasizer Nano ZS90 (Malvern Instruments). The physical properties of the micelles are contained in Supplementary Information Table S6.

### 2.4. In vivo confocal laser scanning microscopy (in vivo CLSM)

A solution of two imaging probes was prepared for each experiment by adjusting their concentrations using *in vitro* calibration to result in roughly equal photoluminescence intensity, as reported previously [23]. Before mixing the probes into a single solution, we calibrated them individually along with the microscope system. Specifically, a sample of each probe was diluted in PBS and collected in a separate capillary tube, which were mounted side-by-side to a microscope slide and imaged using the CLSM to ensure there was no signal bleeding through to the other channel. Additionally, the sensitivity of each channel's photomultiplier tube was adjusted to result in roughly equal signal in each channel and ensure that there was no saturation of the photomultiplier tube's sensor. These relative dilutions and microscope settings were used for the imaging of the probe.

Surgical exposure of the calvarium (Fig. 1) was performed by making a midline vertical incision to expose the calvarium. Then, the periosteum was removed to expose the skull surface. A glass slide was placed over the calvarium and imaging was initiated to select a region of interest (ROI). Then, imaging was started (Supplementary Information Table S7) [5]. After collecting a background image, mice were intravenously co-injected in their tail-vein with BSA (FITC-BSA, Sigma-Aldrich), variously sized dextran (RITC-70 kDa, FITC-10 kDA, FITC-500 kDa and FITC-2000 kDa, Sigma-Aldrich), and/or polymeric micelles (DACHPt/m, 30 nm and 70 nm,) at concentrations between 2 mg/kg and 8 mg/kg (for the dextrans) and total injection volumes of 0.2 mL (see Supplementary Information Table S6 for the parameters of each individual experiment). Concentrations and microscope settings were selected to make the fluorescence signal of each channel equal. All image acquisitions were performed using a Nikon A1R confocal laser scanning microscope system attached to an upright ECLIPSE FN1 (Nikon). For experiments measuring FITC labeled dextrans, a laser 488.5 nm wavelength was used to excite FITC dye and a filter cube 525 nm center wavelength with guaranteed minimum bandwidth of 50 nm for detection of emission. For experiments measuring RITC labeled dextrans, a laser 561.8 nm wavelength was used to excite RITC dye and a filter cube 595 nm center wavelength with guaranteed minimum bandwidth of 50 nm for detection of emission. With the use of separate lasers for excitation and narrow bandpass filters for each channel, there was no observable overlap of detectable signal between FITC and RITC channels.

We quantified transvascular flux using the 2D vascular permeability method described in an experimental protocol previously [24,25]. This method relies on the assumption that the fluorescence intensity in a voxel is interchangeable for the concentration of the probe. The images analyzed for quantification were the collection of a time-series. Imaging was initiated immediately before simultaneous injection of the probes and continued for 10 min, with images being collected every 4.5 s. For qualitative observations, images were collected 80 min after administration, as noted in Supplementary Information Table S7. Images were analyzed using custom analysis software developed in MATLAB (The Mathworks). Vessels were segmented based on intensity and size thresholding. Regions of sinusoids were selected by hand based on vessel morphology. The normalized transvascular flux was calculated in cm/s as $P = (1 - HT)V/S(1/(I_0 - I_b)\cdot dI/dt + 1/K)$, where HT is the tissue hematocrit estimated to be 0.46 in the systemic circulation [26], dI/dt is the derivative of the average fluorescence intensity of the entire region, $I_0$ is the average fluorescence intensity immediately after filling of the vessels by the probe, $I_b$ is the background fluorescence intensity, and K is the time constant of plasma clearance for the probe (BSA [24] and dextrans [27]). V/S is the ratio of tissue volume to the vascular surface area in the image corrected by a factor of 0.79 for light scattering [28]. The transvascular flux values were used in the mathematical models as described in the Supplementary Information.

### 2.5. Statistical analysis

Statistical tests were performed on sets of mice co-injected with a pair of probes. Transvascular fluxes for each probe size in each cohort of mice were compared using a *Z*-test. For each set of flux values in a mouse, one flux was subtracted from the other, and the set of differences in the cohort were compared to 0 using a Z-test. Error bars in graphs

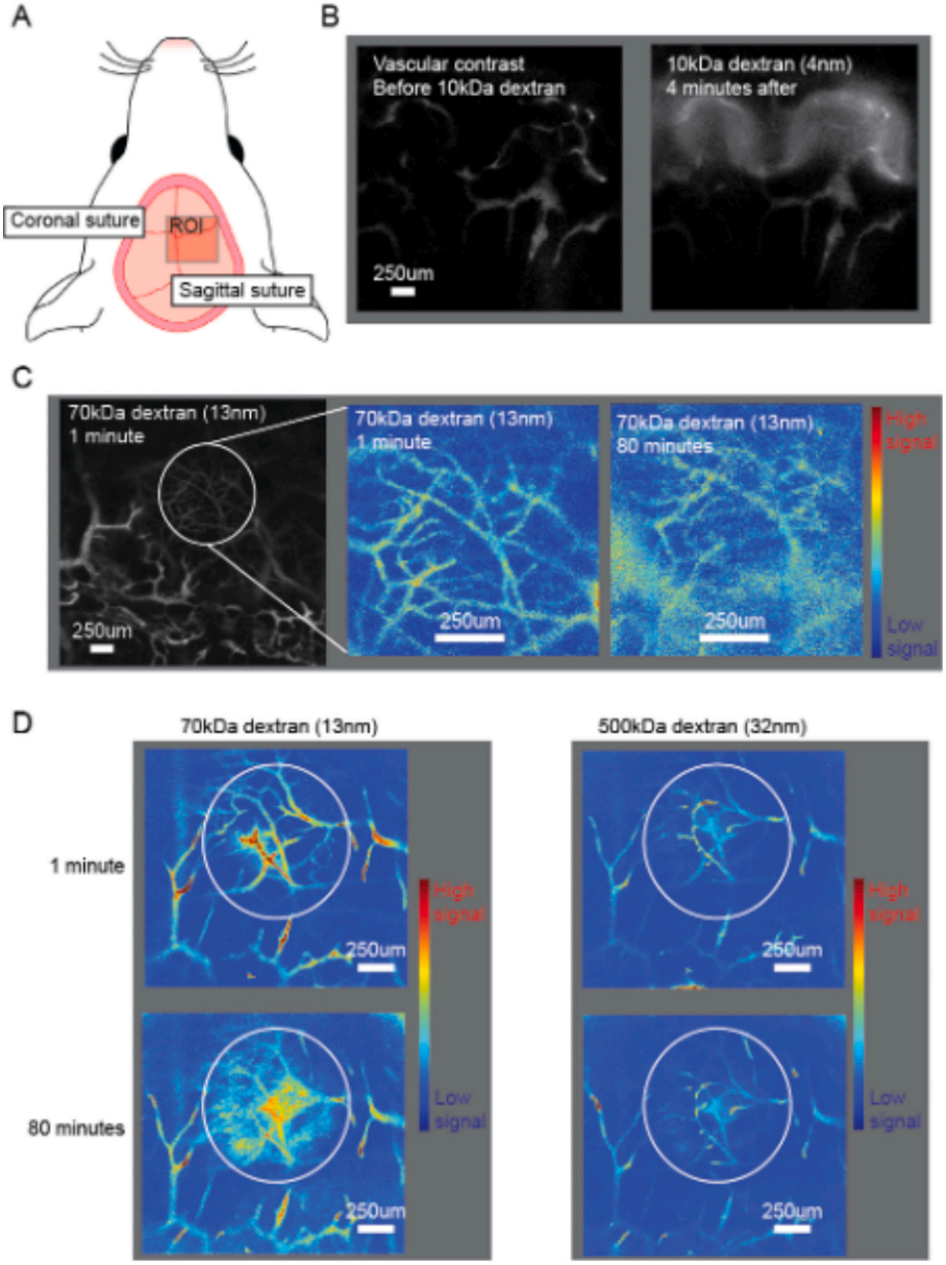

**Fig. 1.** Vessels in the murine calvarial bone marrow are permeable to dextrans up to 500 kDa molecular weight. (A) Schematic of region of interest (ROI, red) along the coronal suture and sagittal suture where intravital imaging occurred. (B—C) Representative confocal intravital microscopy images in the murine calvarium after administration of fluorescent dextrans. (B) While 2000 kDa dextran provided vascular contrast (left panel), 10 kDa dextran immediately extravasated from BM vessels as indicated by the diffuse signal four minutes post-injection (right panel). (C) A low magnification view of the ROI 1-min post-injection 70 kDa dextran (left panel) and a magnified heat map (right panel) indicate vascular contrast, while a heat map from the same region 80 min later displays extensive extravasation as indicated by the diffuse signal (right panel). In heat maps, blue color indicates region with low signal, green color indicates region with moderate signal and red indicates region with high signal. (D) Representative heat maps from confocal intravital microscopy images in the same region of the same murine calvarium after co-injection of 70 kDa and 500 kDa fluorescent dextrans. The white circle marks an area with extravasation. One-minute post-administration there is vascular contrast with some extravasation in the 70 kDa channel (top left panel) and limited extravasation in 500 kDa channel (top right panel). 80 min post-administration, there is extensive extravasation of the 70 kDa dextran (bottom left panel) with limited extravasation of the 500 kDa dextran (bottom right panel). (For interpretation of the references to color in this figure legend, the reader is referred to the web version of this article.)

represent standard error of the mean. The transvascular flux values were used in the mathematical models as described in the Supplementary Information.

## 3. Results

### 3.1. Imaging of bone marrow vessels in murine calvarium

To image the permeability of BM vessels to nanoscale medicine, we exposed the calvarium of mice to perform intravital confocal microscopy at the intersection of the coronal and sagittal sutures (Fig. 1A) to image the same vascularized part of the BM cavity consistently [18,21,29,30].

While imaging in this BM cavity, we intravenously administered a solution of 2000 kDa dextran (Fig. 1B, left panel) for vascular contrast followed by a solution of 10 kDa dextran with a 4 nm hydrodynamic diameter [20]. As expected, the 10 kDa dextran rapidly extravasated from certain vessels, as indicated by the diffuse fluorescent signal (Fig. 1B, right panel).

We repeated the experiment using 70 kDa dextrans [20], which unlike 10 kDa dextrans are larger than the accepted pore cutoff size of BM sinusoids. These 70 kDa dextrans remained in the vasculature at 1-min post-injection (Fig. 1C, left and center panels), but after 80 min there was substantial signal outside of BM vessels (Fig. 1C, right panel). Because 70 kDa dextrans extravasated, we repeated the experiment while co-injecting dextrans with 70 kDa and 500 kDa with a hydrodynamic diameter of 32 nm [20] (Fig. 1*D*). As before, 70 kDa dextrans extravasated slightly at short times and extensively at longer times (Fig. 1D, left panels), whereas the extravasation of the 500 kDa dextran appeared lower than that of the 70 kDa dextran (Fig. 1D, right panels). Thus, these qualitative observations indicate dextrans up to at least 500 kDa extravasate from BM vessels.

### 3.2. *Imaging of sinusoids and non-sinusoids in murine calvarium*

Given that previous studies showed that sinusoids and non-sinusoids in the BM have different permeabilities to 70 kDa dextrans [5], we next sought to distinguish vessel sub-populations and confirm their different permeabilities. Sinusoids were discriminated from non-sinusoids based on the following characteristics: honeycomb branching and high diameter-to-length ratios. Then, we injected 70 kDa dextran while imaging in the calvarium (Fig. 2A), and manually segmented sinusoids (Fig. 2B) from non-sinusoids (Fig. 2C) based on the above criteria. The penetration rates were quantified as transvascular mass flux per vascular surface area and transvascular concentration difference during the first 10 min post-injection [23–25]. This is often called effective permeability or transvascular flux [23]. We found that the transvascular flux of 70 kDa dextrans indicated hyperpermeability. Moreover, the transvascular flux was 2-fold higher in sinusoids than in non-sinusoids (Fig. 2D), consistent with previous measurements (Supplementary Information Fig. S1).

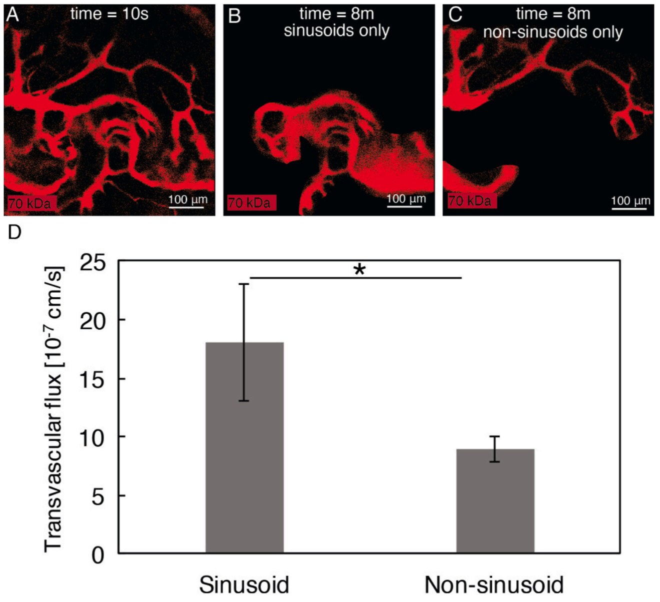

**Fig. 2.** Sinusoids are leakier to 70 kDa dextrans than non-sinusoids. (A-C) Representative confocal intravital microscopy images in the same region of the same murine calvarium show 70 kDa dextrans around sinusoids and non-sinusoids. (A) An image 10 s post-injection defines the vessels. (B) After 8 min, sinusoids leaked dextran. (C) Dextran signal remains within non-sinusoids. (D) Sinusoids are leakier to 70 kDa (~13 nm) dextrans than non-sinusoids, as measured by effective permeability also known as transvascular flux. Sinusoids have 2-fold faster flux ($P = 0.04$, *Z*-test). Animal number, $n = 19$.

### 3.3. *10 kDa dextrans extravasate faster from BM vessels than larger 70 kDa dextrans*

We next sought to compare the penetration rates of 70 kDa dextran with 10 kDa dextran, which has a hydrodynamic diameter of 4 nm [20], to test the permselectivity of BM vessels to differently sized macromolecules. We imaged continuously in a single region in the calvarium of mice before, during and after simultaneous injection with 10 kDa dextrans and 70 kDa dextrans and observed regions of extravasation (Fig. 3). Qualitative observation indicated that certain vessels, that were not leaky to 70 kDa dextrans, were leaky to 10 kDa dextrans within 8 min post-injection (Fig. 3A). Measuring the permeability, we found a trend that BM sinusoids were almost 2.1-fold more permeable to 10 kDa

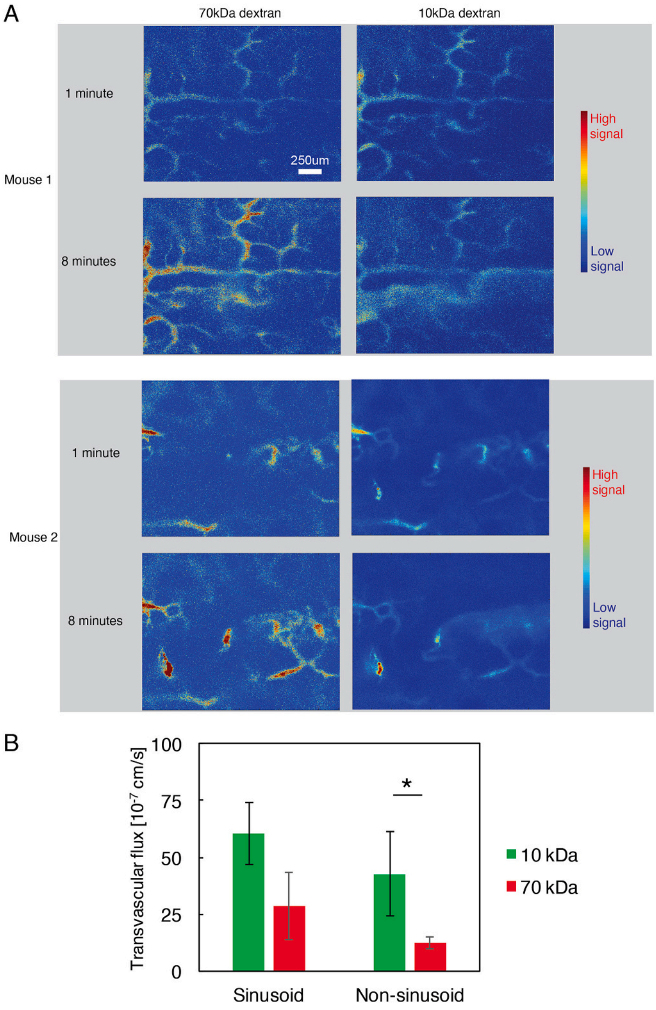

**Fig. 3.** BM non-sinusoids are permselective to dextrans with 10 kDa and 70 kDa molecular weights. (A) Representative heat maps from confocal intravital microscopy images from two mice (top and bottom gray boxes) show the distribution of florescent 70 kDa dextrans (left panels) and 10 kDa dextrans (right panels) one minute (top rows) and eight minutes (bottom rows) post-administration. Blue color indicates region with low signal, green color indicates region with moderate signal and red indicates region with high signal. (B) Penetration rates (transvascular flux) for dextrans in BM. Sinusoids had a trend faster flux to 10 kDa compared to 70 kDa dextran by a factor of 2.1 ($P = 0.07$, *Z*-test). The 4-fold difference was significant in non-sinusoids ($P = 0.04$, *Z*-test). Animal number, $n = 6$. (For interpretation of the references to color in this figure legend, the reader is referred to the web version of this article.)

than 70 kDa dextrans and a statistically significant 3.4-fold difference between the dextrans in non-sinusoids (Fig. 3B). Although BM vessels are hyperpermeable to both dextrans, there is a higher permselectivity in BM vessels than tumor vessels, which have permeability that only varies 2-fold between 25 kDa and 160 kDa [31], although size dependence of NC penetration varies with tumor type [22,32].

### *3.4. 70 kDa dextrans extravasate faster from BM vessels than stiffer albumin*

BM sinusoids are part of the reticuloendothelial system (RES) and, thus, have high levels of endocytosis. Because albumin is a transport protein with ligand binding sites and has high levels of cellular engagement, we hypothesized that albumin may pass into BM extravascular space quicker than a similarly sized dextran. Indeed, albumin-bound paclitaxel induces BM toxicity in patients (Supplementary Information Table S5). To test our hypothesis, we simultaneously injected fluorescently-labeled BSA and 70 kDa dextran. Although the hydrodynamic diameter of 70 kDa dextran is higher than that of BSA (13 nm *vs.* 8 nm), dextran is more flexible, which is a property that facilitates extravasation and penetration [33,34]. However, if active transport of albumin facilitates transvascular transport in the period of observation, then BSA extravasation rates could be higher. Our results showed larger regions of extravasation of the 70 kDa probe compared to BSA in the same mice (Fig. 4A). Moreover, we found a trend, but no statistically significant difference, in the effective permeability rates of sinusoids to 70 kDa dextran than BSA (Fig. 4B). In non-sinusoids, the effective permeability rates for 70 kDa dextran were 1.8-fold higher than that of BSA. These results suggest that rigidity or binding of the macromolecules may play a larger role in hindering the passive transport than the hydrodynamic diameter in this size range. Also, these observations support the notion that passive – not active – transport facilitates the flux of albumin and albumin-sized macromolecules at short times on the order of minutes. Typically, vessels in tumors are more permeable to BSA than normal vessels of the same organs by a factor of 5–10 [24,28,35,36] – even in the liver, which is full of leaky sinusoids [37]. This is true in the bone marrow as well [21]. Surprisingly, our results when compared with historical data [24], suggest that healthy BM sinusoids may be more permeable to BSA than vessels in various non-BM tumors, and the permeability of BM non-sinusoids to BSA could be comparable to that of tumor vessels.

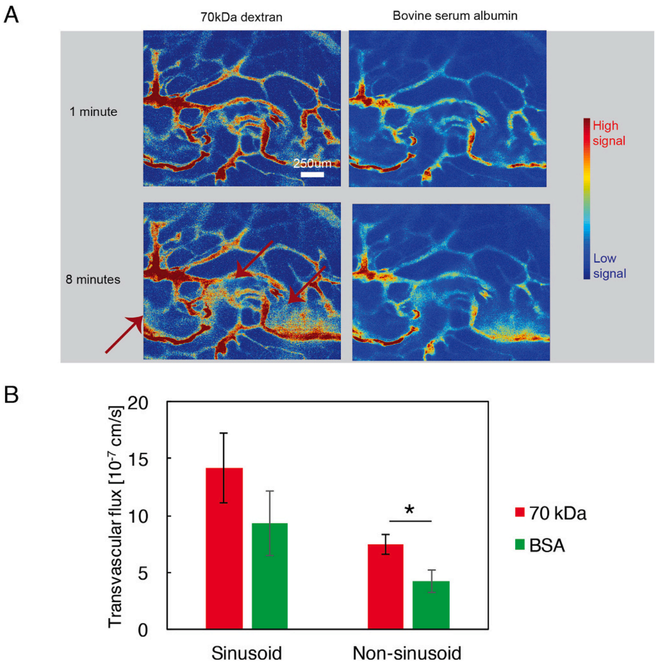

**Fig. 4.** 70 kDa dextrans extravasate faster from BM vessels than smaller, stiffer albumin. (A) Representative heat maps from confocal intravital microscopy images of calvarial bone marrow from a mouse with injected with florescent RITC labeled 70 kDa dextrans (left panels) and FITC labeled bovine serum albumin (BSA, right panels) one minute (top panels) and eight minutes (bottom panels) post-administration. Blue color indicates region with low signal, green color indicates region with moderate signal and red indicates region with high signal. Red arrows indicate regions with higher extravasation of 70 kDa dextran compared to BSA. (B) Transvascular flux of 70 kDa dextrans in non-sinusoids was higher than that of BSA ($P$ < 10–4, $Z$-test). Animal number, $n = 8$. (For interpretation of the references to color in this figure legend, the reader is referred to the web version of this article.)

### *3.5. 70 kDa dextrans extravasate faster from BM vessels than larger 500 kDa dextrans*

Next, we hypothesized that there is permselectivity above probe sizes of 13 nm. To test this, we simultaneously injected 70 kDa (∼13 nm hydrodynamic diameter [20]) and 500 kDa dextrans (32 nm hydrodynamic diameter [20]) while imaging in the mouse calvarium (Fig. 5A). We found statistically significant differences in that 70 kDa dextran penetrated 2.2-fold faster from BM sinusoids and non-sinusoids than 500 kDa dextran (Fig. 5B). Thus, BM sinusoids and non-sinusoids are permselective to probes sized up to 32 nm. Observing at more than an hour post-injection, we found that 70 kDa dextran substantially extravasated from certain vessels, while 500 kDa remained in the vessels.

### *3.6. Mathematical model predicts average and maximum vessel wall pore diameters*

To gain insight into the mechanism of transport and the size of pores in BM vessels, we employed a mathematical model describing passive fluid and macromolecule transport (Supplementary Information Fig. S6) [23,38–41]. We formulated and solved a parameter estimation problem for the effective vessel wall pore size (*i.e.*, diameter) associated with the model (Supplementary Information). We generated transient spatial average probe concentration profiles based on the experimentally obtained effective permeabilities. Then, we used these profiles to determine an effective vessel pore size corresponding to the optimal fit of the model-predicted concentration profiles to the experimental data. We performed this analysis for the data obtained from each mouse at two probe sizes. The 4 nm probe predicted unrealistically large pore sizes that did not fit the data well (exhibiting bias in the fit), which suggests that the transport of the 4 nm probe is purely convective and not hindered sterically (Supplementary Figs. S3(a)-(b)). For the other probes sized up to 32 nm, the model's predictions fit the data very well with no observable bias, suggesting that the transport was passive and occurred through a combination of diffusion and convection (Supplementary Information Figs. S3(c)-(d), S4, and S5). The average effective pore sizes were 47 nm and 37 nm for sinusoids and non-sinusoids, respectively (Fig. 6 A). We note that since the mathematical model assumes a fixed hydrodynamic diameter for macromolecules, predicted effective pore sizes could be larger for more flexible macromolecules that are sterically hindered and undergo conformation changes. This is not expected to be the case for the macromolecules considered in this study.

We then applied an alternative approach whereby only the mathematical model describing hindered passive transport of large molecules in liquid-filled pores [42] (Supplementary Information Transvascular Flux (Pore Theory) section) is considered to determine the maximum effective pore size. Using the data from the 32 nm dextran permeability experiments, we estimated the largest pores to be 61 nm and 53 nm for sinusoids and non-sinusoids, respectively (Fig. 6B and Supplementary Information Figs. S5 and S7). Thus, the model results are consistent with the notion that the probes passed the vessel wall passively since both the macroscopic solute transport model and the pore transport model fit the

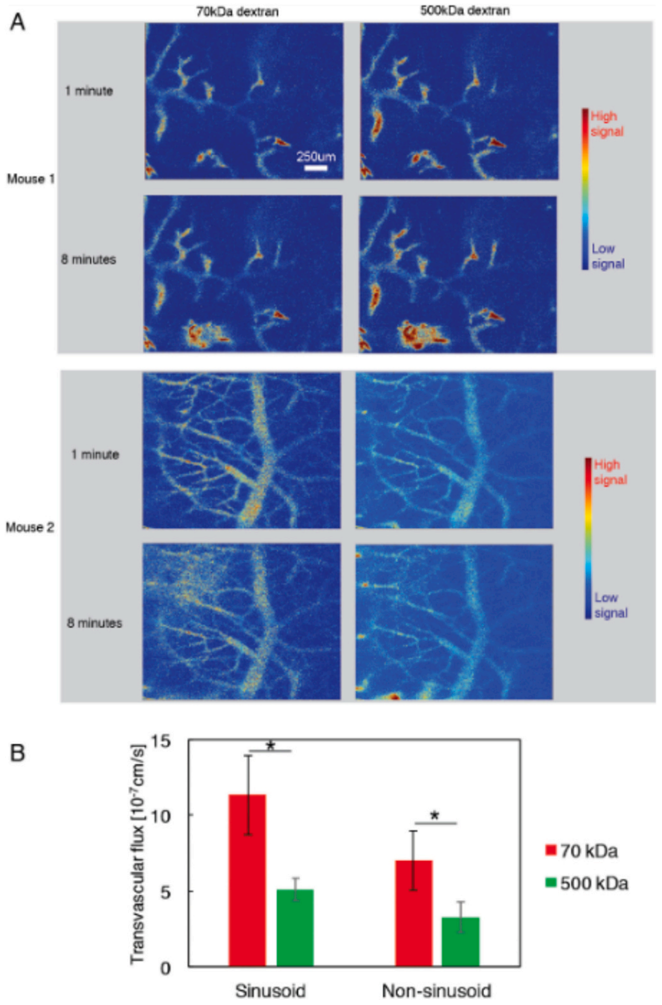

**Fig. 5.** BM sinusoids are permselective to dextrans with 70 kDa and 500 kDa molecular weights. (A) Representative heat maps from confocal intravital microscopy images from two mice (top and bottom gray boxes) show the distribution of florescent 70 kDa dextrans (left panels) and 500 kDa dextrans (right panels) one minute (top rows) and eight minutes (bottom rows) post-administration. Blue color indicates region with low signal, green color indicates region with moderate signal and red indicates region with high signal. (B) Penetration rates (transvascular flux) for dextrans in BM. Both sinusoids and non-sinusoids have faster flux of 70 kDa compared to 500 kDa dextran by a factor of 2.2 ($P < 0.0001$, $Z$-test). Animal number, $n = 5$. (For interpretation of the references to color in this figure legend, the reader is referred to the web version of this article.)

data well. Furthermore, the macroscopic solute transport model's ability to effectively fit the transport data of all probes other than 4 nm suggest steric hindrance occurs and is significant for larger probes. Indeed, diffusive hindrance is highly sensitive to particle size when it is between 20 and 40 % of the pore size [23] and the second smallest probe we assayed, BSA, is ~20 % of the maximum pore size of non-sinusoids.

To confirm the pore size predictions of our model, we *co*-injected polymeric micelles of varied sizes, each loaded with 1,2-diaminocyclohexane-platinum(II) (DACHPt), which is the parent complex of oxaliplatin, and observed their microdistribution in murine calvarial bone marrow in real time [22] (Fig. 6C). We found regions where 30 nm micelles extravasated greater than the 70 nm micelles. These translational findings are consistent with our model and experimental data indicating that the physiological effective pore cutoff size available for transport in BM vessels – sinusoidal or not – is larger than 5 nm.

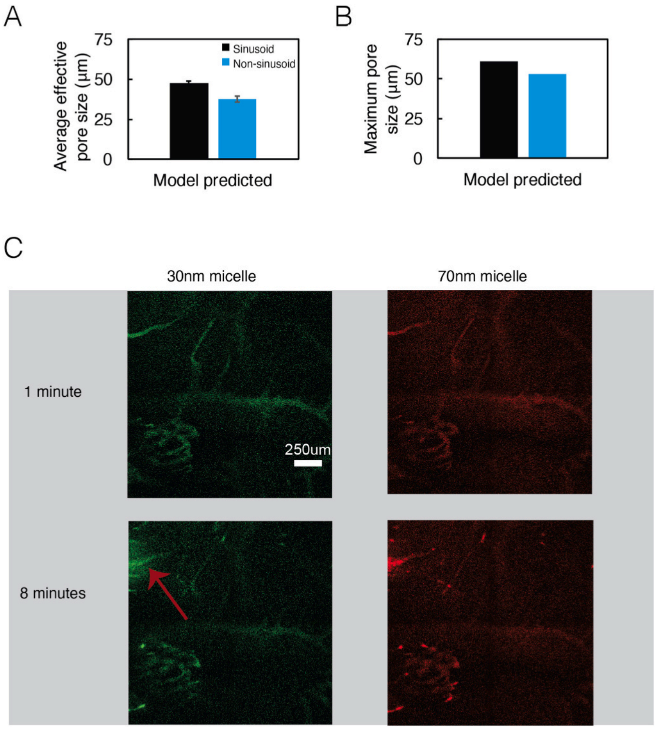

**Fig. 6.** Model results and penetration of drug-loaded polymeric micelles. (A) Average of predicted effective vessel pore sizes. Sinusoidal pores (black) were generally predicted to be larger than non-sinusoids (blue). (B) The maximum pore size predicted by a model based on the permeabilities of the 500 kDa (32 nm) dextran. (C) Representative images from confocal intravital microscopy images of calvarial bone marrow from a mouse with injected with florescent 30 nm polymeric micelles (left panels) and 70 nm polymeric micelles (BSA, right panels) one minute (top panels) and eight minutes (bottom panels) post-administration. Red arrow indicates region with higher extravasation of 30 nm micelles. (For interpretation of the references to color in this figure legend, the reader is referred to the web version of this article.)

## 4. Discussion

Using intravital microscopy, we observed extravasation from BM vessels of all probes assessed (4 nm to 32 nm hydrodynamic diameters). We quantified the rate of the extravasation from sinusoids and non-sinusoids (Supplementary Information Fig. S8) and found them to be permselective at least up to 32 nm (Supplementary Information Fig. S7). Using a mathematical model, the effective pore sizes in the vessel wall of sinusoids and non-sinusoids were found to be 47 nm and 37 nm, respectively, while the theoretical maximum pore sizes were 61 nm and 53 nm. The model suggests that all probes larger than the 4 nm dextran encountered steric hindrance. In comparing translational chemotherapy-loaded polymeric micelles of different sizes, we found that a 30 nm micelle, which is smaller than the model predicted pore sizes, extravasated readily while a 70 nm micelle, which is larger, did not. These results highlight the importance of size when designing NCs to target or avoid BM during passive circulation.

It should be noted that we measured permeability with images collected during and up to 10 min after injection, but the accumulation of NCs over several days ultimately accounts for therapeutic and/or adverse effects of NCs on cells in the BM. Nonetheless, accumulation also depends on circulation time and other factors, such as active transport by BM RES. Thus, accumulation studies cannot reveal information about pore size nor size-dependence of NCs on passive transport. Here, in contrast to previous reports that suggest that NC or macromolecule BM accumulation occurs because of active transport after long circulation [11], we found permeability rates similar to tumor vessels based on intravital microscopy measurements. Our model assumes that the probes do not interact with each other. Additionally, while the intravenous administration of dextrans might decrease permselectivity of healthy capillaries [43], we still could observe permselectivity in BM vessels. While an intravenous injection could increase plasma volume thereby promoting more plasma flow from vessels to extravascular space, this situation is identical to the physiological state after drug administration. Our findings should be confirmed with various classes of nanocarriers and host model systems. The results can be expected to vary based on the physicochemical properties of the nanocarriers and host species.

Rates of BM toxicities to NCs and macromolecule therapeutics are high in cancer, so these findings can have implications for radiation therapy [44] and immunotherapy [45]. Although NCs reduce the hematological toxicity of small-molecule chemotherapies (Supplementary Information Table 5 – top two rows), NC-based chemotherapies like albumin-based nab-paclitaxel (~10 nm in circulation [23]) and liposomal irinotecan (~90 nm) induce hematological toxicity compared to no treatment (Supplementary Information Table S5 – bottom two rows). These studies are consistent with positron emission topography studies of labeled liposomes that demonstrate BM accumulation [46]. Additionally, antibody-drug conjugates induce high levels of BM toxicities through unclear mechanisms [47]. In 2005 in the USA, chemotherapy-induced neutropenia – one type of hematological toxicity – was estimated to cause 4080 deaths and cost more than $800,000,000 in hospital visits per year [48], so if NCs could better avoid the BM, they could alleviate some of this burden. Based on these studies, we hypothesized that BM vessels might feature permselectivity thresholds and a pore cutoff size larger than 5 nm. Our findings offer valuable guidance for researchers aiming to design nanocarriers that selectively target or avoid the bone marrow with greater precision. For example, highly permeable formulations are likely to achieve greater bone marrow accumulation compared to less permeable ones, enhancing therapeutic efficacy for bone marrow-targeted treatments. However, this same accumulation could increase the risk of toxicity in the case of cytotoxic nanomedicines. These insights pave the way for developing more effective targeted therapies and safer clinical nanomedicines, particularly in cancer treatment, by enabling precise control over nanocarrier biodistribution. Future studies may investigate whether a NC size window exists to increase accumulation in tumors relative to BM.

## 5. Conclusions

Based on intravital microscopy observation, we found that the extravasation rates of various probes from bone marrow (BM) vessels were size-dependent, with smaller probes extravasating more readily than larger ones. Using mathematical models, we estimated effective pore sizes for sinusoids and non-sinusoids to be 47 nm and 37 nm, respectively, with maximum pore sizes of 61 nm and 53 nm. These predictions were validated by demonstrating that 70 nm polymeric micelles extravasated less readily than 30 nm micelles. Given the high rates of bone marrow toxicities associated with NC-based chemotherapies, optimizing NC size to avoid BM could potentially reduce adverse effects and enhance therapeutic outcomes. Future research should aim to identify an optimal NC size range that maximizes tumor accumulation while minimizing BM toxicity.

## CRediT authorship contribution statement

**John D. Martin:** Writing – original draft, Investigation, Formal analysis, Data curation. **Kazuko Toh:** Investigation, Formal analysis. **Margaret R. Martin:** Formal analysis. **Pengwen Chen:** Writing – review & editing, Investigation, Formal analysis, Data curation. **Chenyu Wang:** Methodology, Formal analysis. **Kazunori Igarashi:** Investigation. **Fotios Mpekris:** Methodology, Investigation. **Triantafyllos Stylianopoulos:** Resources, Methodology. **Matthew D. Stuber:** Writing – review & editing, Methodology, Formal analysis, Data curation. **Kazunori Kataoka:** Writing – review & editing, Supervision, Funding acquisition. **Horacio Cabral:** Writing – review & editing, Supervision, Resources, Project administration, Funding acquisition, Data curation, Conceptualization.

## Acknowledgements

We thank Dr. Vikash P. Chauhan for helpful discussions. This work was supported by Grants-in-Aid for Scientific Research A (23H00546; H. C.), Grants-in-Aid for Exploratory Research (22 K19541; H.C.), and the Fund for the Promotion of Joint International Research (Fostering Joint International Research (B), 21KK0197; H.C.), from the Japan Society for the Promotion of Science (JSPS). This work was also partially supported by the AMED Seeds A grant (23ym0126805j0002; H.C.), the University of Connecticut (M.D.S.) and the Pratt & Whitney Associate Professorship in Advanced Systems Engineering (M.D.S.). This work was also supported by fellowships from the Japan Society for the Promotion of Science (Nos. P16731 and PE14787 to J.D.M), the European Research Council Grant 336839 and INFRASTRUCTURE/1216/0052 co-financed by the European Regional Development Fund and the Republic of Cyprus through the Research Promotion Foundation (T.S.).

## Appendix A. Supplementary data

Supplementary data to this article can be found online at https://doi.org/10.1016/j.jconrel.2025.113669.

## Data availability

Data will be made available on request.

## References

[1] S.J. Morrison, D.T. Scadden, The bone marrow niche for haematopoietic stem cells, Nature 505 (7483) (2014) 327–334.
[2] X. Liu, J. Jiang, R. Chan, Y. Ji, J. Lu, Y.-P. Liao, M. Okene, J. Lin, P. Lin, C. H. Chang, X. Wang, I. Tang, E. Zheng, W. Qiu, Z.A. Wainberg, A.E. Nel, H. Meng, Improved efficacy and reduced toxicity using a custom-designed irinotecan-delivering silicasome for orthotopic colon cancer, ACS Nano 13 (1) (2019) 38–53.
[3] H. Cabral, J. Li, K. Miyata, K. Kataoka, Controlling the biodistribution and clearance of nanomedicines, Nat. Rev. Bioeng. 2 (2024) 214–232.
[4] M. Krohn-Grimberghe, M.J. Mitchell, M.J. Schloss, O.F. Khan, G. Courties, P. P. Guimaraes, D. Rohde, S. Cremer, P.S. Kowalski, Y. Sun, M. Tan, J. Webster, K. Wang, Y. Iwamoto, S.P. Schmidt, G.R. Wojtkiewicz, R. Nayar, V. Frodermann, M. Hulsmans, A. Chung, F.F. Hoyer, F.K. Swirski, R. Langer, D.G. Anderson, M. Nahrendorf, Nanoparticle-encapsulated siRNAs for gene silencing in the haematopoietic stem-cell niche, Nat. Biomed. Eng. 4 (11) (2020) 1076–1089.
[5] T. Itkin, S. Gur-Cohen, J.A. Spencer, A. Schajnovitz, S.K. Ramasamy, A.P. Kusumbe, G. Ledergor, Y. Jung, I. Milo, M.G. Poulos, Distinct bone marrow blood vessels differentially regulate haematopoiesis, Nature 532 (7599) (2016) 323–328.
[6] M. Acar, K.S. Kocherlakota, M.M. Murphy, J.G. Peyer, H. Oguro, C.N. Inra, C. Jaiyeola, Z. Zhao, K. Luby-Phelps, S.J. Morrison, Deep imaging of bone marrow shows non-dividing stem cells are mainly perisinusoidal, Nature 526 (7571) (2015) 126–130.
[7] M. Tavassoli, W.H. Crosby, Fate of the nucleus of the marrow erythroblast, Science 179 (4076) (1973) 912–913.
[8] P.P. De Bruyn, S. Michelson, T.B. Thomas, The migration of blood cells of the bone marrow through the sinusoidal wall, J. Morphol. 133 (4) (1971) 417–437.
[9] F.R. Campbell, Ultrastructural studies of transmural migration of blood cells in the bone marrow of rats, mice and guinea pigs, Am. J. Anat. 135 (4) (1972) 521–535.
[10] R.K. Jain, T. Stylianopoulos, Delivering nanomedicine to solid tumors, Nat. Rev. Clin. Oncol. 7 (11) (2010) 653–664.
[11] H. Sarin, Physiologic upper limits of pore size of different blood capillary types and another perspective on the dual pore theory of microvascular permeability, J. Angiogenes. Res. 2 (1) (2010) 1.
[12] M. Tavassoli, M. Shaklai, Absence of tight junctions in endothelium of marrow sinuses: possible significance for marrow cell egress, Br. J. Haematol. 41 (3) (1979) 303–307.
[13] H.E. Daldrup, T.M. Link, S. Blasius, A. Strozyk, S. Könemann, H. Jürgens, E. J. Rummeny, Monitoring radiation-induced changes in bone marrow histopathology with ultra small superparamagnetic iron oxide (USPIO) enhanced MRI, J. Magn. Reson. Imaging 9 (5) (1999) 643–652.
[14] H. Daldrup-Link, T. Link, E. Rummeny, C. August, S. Könemann, H. Jürgens, W. Heindel, Assessing permeability alterations of the blood–bone marrow barrier

due to total body irradiation: in vivo quantification with contrast enhanced magnetic resonance imaging, Bone Marrow Transplant. 25 (1) (2000) 71.
[15] L. Ilium, S. Davis, Targeting of colloidal particles to the bone marrow, Life Sci. 40 (16) (1987) 1553–1560.
[16] S. Davis, L. Ilium, S.M. Moghimi, M. Davies, C. Porter, I. Muir, A. Brindley, N. Christy, M. Norman, P. Williams, Microspheres for targeting drugs to specific body sites, J. Control. Release 24 (1–3) (1993) 157–163.
[17] A.A. Martindale, J.M. Papadimitriou, J.H. Turner, Technetium-99m antimony colloid for bone-marrow imaging, J. Nucl. Med. 21 (11) (1980) 1035–1041.
[18] K. Vandoorne, D. Rohde, H.-Y. Kim, G. Courties, G. Wojtkiewicz, L. Honold, F. F. Hoyer, V. Frodermann, R. Nayar, F. Herisson, Imaging the vascular bone marrow niche during inflammatory stress, Circ. Res. 123 (4) (2018) 415–427.
[19] J.D. Martin, R.M. Lanning, V.P. Chauhan, M.R. Martin, A.S. Mousa, W.S. Kamoun, H.-S. Han, H. Lee, T. Stylianopoulos, M.G. Bawendi, D.G. Duda, E.B. Brown, T. P. Padera, D. Fukumura, R.K. Jain, Multiphoton phosphorescence quenching microscopy reveals kinetics of tumor oxygenation during anti-angiogenesis and angiotensin signaling inhibition, Clin. Cancer Res. 28 (14) (2022) 3076–3090.
[20] J.K. Armstrong, R.B. Wenby, H.J. Meiselman, T.C. Fisher, The hydrodynamic radii of macromolecules and their effect on red blood cell aggregation, Biophys. J. 87 (6) (2004) 4259–4270.
[21] D. Passaro, A. Di Tullio, A. Abarrategi, K. Rouault-Pierre, K. Foster, L. Ariza-McNaughton, B. Montaner, P. Chakravarty, L. Bhaw, G. Diana, Increased vascular permeability in the bone marrow microenvironment contributes to disease progression and drug response in acute myeloid leukemia, Cancer Cell 32 (3) (2017) 324–341 (e6).
[22] H. Cabral, Y. Matsumoto, K. Mizuno, Q. Chen, M. Murakami, M. Kimura, Y. Terada, M.R. Kano, K. Miyazono, M. Uesaka, N. Nishiyama, K. Kataoka, Accumulation of sub-100 nm polymeric micelles in poorly permeable tumours depends on size, Nat. Nanotechnol. 6 (12) (2011) 815–823.
[23] V.P. Chauhan, T. Stylianopoulos, J.D. Martin, Z. Popovic, O. Chen, W.S. Kamoun, M.G. Bawendi, D. Fukumura, R.K. Jain, Normalization of tumour blood vessels improves the delivery of nanomedicines in a size-dependent manner, Nat. Nanotechnol. 7 (6) (2012) 383–388.
[24] E.F. Meijer, J.W. Baish, T.P. Padera, D. Fukumura, Measuring vascular permeability in vivo, in: The Tumor Microenvironment, Springer, 2016, pp. 71–85.
[25] J.D. Martin, M. Panagi, C. Wang, T.T. Khan, M.R. Martin, C. Voutouri, K. Toh, P. Papageorgis, F. Mpekris, C. Polydorou, G. Ishii, S. Takahashi, N. Gotohda, T. Suzuki, M.E. Wilhelm, V.A. Melo, S. Quader, J. Norimatsu, R.M. Lanning, M. Kojima, M.D. Stuber, T. Stylianopoulos, K. Kataoka, H. Cabral, Dexamethasone increases cisplatin-loaded Nanocarrier delivery and efficacy in metastatic breast cancer by normalizing the tumor microenvironment, ACS Nano 13 (6) (2019) 6396–6408.
[26] B. Schuler, M. Arras, S. Keller, A. Rettich, C. Lundby, J. Vogel, M. Gassmann, Optimal hematocrit for maximal exercise performance in acute and chronic erythropoietin-treated mice, Proc. Natl. Acad. Sci. 107 (1) (2010) 419–423.
[27] I.W. Kellaway, L. Seale, P.S. Spencer, The in vitro characterization and biostability of 99m Tc-dextran and its accumulation within the inflamed paws of adjuvant-induced arthritic rats, Pharm. Res. 12 (4) (1995) 588–593.
[28] F. Yuan, H.A. Salehi, Y. Boucher, U.S. Vasthare, R.F. Tuma, R.K. Jain, Vascular permeability and microcirculation of gliomas and mammary carcinomas transplanted in rat and mouse cranial windows, Cancer Res. 54 (17) (1994) 4564–4568.
[29] I.B. Mazo, J.-C. Gutierrez-Ramos, P.S. Frenette, R.O. Hynes, D.D. Wagner, U.H. Von Andrian, Hematopoietic progenitor cell rolling in bone marrow microvessels: parallel contributions by endothelial selectins and vascular cell adhesion molecule 1, J. Exp. Med. 188 (3) (1998) 465–474.
[30] H.-S. Han, E. Niemeyer, Y. Huang, W.S. Kamoun, J.D. Martin, J. Bhaumik, Y. Chen, S. Roberge, J. Cui, M.R. Martin, Quantum dot/antibody conjugates for in vivo cytometric imaging in mice, Proc. Natl. Acad. Sci. 112 (5) (2015) 1350–1355.
[31] F. Yuan, M. Dellian, D. Fukumura, M. Leunig, D.A. Berk, V.P. Torchilin, R.K. Jain, Vascular permeability in a human tumor xenograft: molecular size dependence and cutoff size, Cancer Res. 55 (17) (1995) 3752–3756.
[32] J.D. Martin, H. Cabral, T. Stylianopoulos, R.K. Jain, Improving cancer immunotherapy using nanomedicine: progress, opportunities and challenges, Nat. Rev. Clin. Oncol. 17 (2020) 251–266.
[33] A. Pluen, P.A. Netti, R.K. Jain, D.A. Berk, Diffusion of macromolecules in agarose gels: comparison of linear and globular configurations, Biophys. J. 77 (1) (1999) 542–552.
[34] V.P. Chauhan, R.K. Jain, Strategies for advancing cancer nanomedicine, Nat. Mater. 12 (11) (2013) 958–962.
[35] Y. Tsuzuki, C. Mouta Carreira, M. Bockhorn, L. Xu, R.K. Jain, D. Fukumura, Pancreas microenvironment promotes VEGF expression and tumor growth: novel window models for pancreatic tumor angiogenesis and microcirculation, Lab. Investig.; J. Tech. Methods Pathol. 81 (10) (2001) 1439–1451.
[36] W.L. Monsky, D. Fukumura, T. Gohongi, M. Ancukiewcz, H.A. Weich, V. P. Torchilin, F. Yuan, R.K. Jain, Augmentation of transvascular transport of macromolecules and nanoparticles in tumors using vascular endothelial growth factor, Cancer Res. 59 (16) (1999) 4129–4135.
[37] D. Fukumura, F. Yuan, W.L. Monsky, Y. Chen, R.K. Jain, Effect of host microenvironment on the microcirculation of human colon adenocarcinoma, Am. J. Pathol. 151 (3) (1997) 679–688.
[38] L.T. Baxter, R.K. Jain, Transport of fluid and macromolecules in tumors. I. Role of interstitial pressure and convection, Microvasc. Res. 37 (1) (1989) 77–104.
[39] L.T. Baxter, R.K. Jain, Transport of fluid and macromolecules in tumors. II. Role of heterogeneous perfusion and lymphatics, Microvasc. Res. 40 (2) (1990) 246–263.
[40] L.T. Baxter, R.K. Jain, Transport of fluid and macromolecules in tumors. III. Role of binding and metabolism, Microvasc. Res. 41 (1) (1991) 5–23.
[41] L.T. Baxter, R.K. Jain, Transport of fluid and macromolecules in tumors. IV. A microscopic model of the perivascular distribution, Microvasc. Res. 41 (2) (1991) 252–272.
[42] W. Deen, Hindered transport of large molecules in liquid-filled pores, AICHE J. 33 (9) (1987) 1409–1425.
[43] B. Rippe, B. Haraldsson, Transport of macromolecules across microvascular walls: the two-pore theory, Physiol. Rev. 74 (1) (1994) 163–219.
[44] H. Li, Q. Gong, K. Luo, Biomarker-driven molecular imaging probes in radiotherapy, Theranostics 14 (10) (2024) 4127–4146.
[45] J. Liu, Y. Bai, Y. Li, X. Li, K. Luo, Reprogramming the immunosuppressive tumor microenvironment through nanomedicine: an immunometabolism perspective, eBioMedicine 107 (2024) 105301.
[46] H. Lee, A.F. Shields, B.A. Siegel, K.D. Miller, I. Krop, C.X. Ma, P.M. LoRusso, P. N. Munster, K. Campbell, D.F. Gaddy, S.C. Leonard, E. Geretti, S.J. Blocker, D. B. Kirpotin, V. Moyo, T.J. Wickham, B.S. Hendriks, 64Cu-MM-302 positron emission tomography quantifies variability of enhanced permeability and retention of nanoparticles in relation to treatment response in patients with metastatic breast cancer, Clin. Cancer Res. 23 (15) (2017) 4190–4202.
[47] H. Zhao, S. Gulesserian, M.C. Malinao, S.K. Ganesan, J. Song, M.S. Chang, M. M. Williams, Z. Zeng, M. Mattie, B.A. Mendelsohn, A potential mechanism for ADC-induced neutropenia: role of neutrophils in their own demise, Mol. Cancer Ther. 16 (9) (2017) 1866–1876.
[48] V. Caggiano, R.V. Weiss, T.S. Rickert, W.T. Linde-Zwirble, Incidence, cost, and mortality of neutropenia hospitalization associated with chemotherapy, Cancer 103 (9) (2005) 1916–1924.

# Supplementary Information

## BONE MARROW VESSELS ARE HYPERPERMEABLE TO MACROMOLECULES AND NANOSCALE MEDICINE IN A SIZE-DEPENDENT MANNER

John D. Martin,[†] Kazuko Toh,[‡] Margaret R. Martin,[†] Pengwen Chen,[†] Chenyu Wang,[¶] Kazunori Igarashi,[†] Fotios Mpekris,[§] Triantafyllos Stylianopoulos,[§] Matthew D. Stuber,[*,¶] Kazunori Kataoka,[*,‡] and Horacio Cabral[*,†]

†*Department of Bioengineering, Graduate School of Engineering, The University of Tokyo, Bunkyo, Tokyo, Japan*

‡*Innovation Center of NanoMedicine, Kawasaki Institute of Industrial Promotion, Kawasaki, Kanagawa, Japan*

¶*Process Systems and Operations Research Laboratory, Department of Chemical and Biomolecular Engineering, University of Connecticut, Storrs, CT, USA*

§*Cancer Biophysics Laboratory, Department of Mechanical and Manufacturing Engineering, University of Cyprus, Nicosia, Cyprus*

E-mail: stuber@alum.mit.edu(MDS); kataoka@ifi.u-tokyo.ac.jp(KK); horacio@bmw.t.u-tokyo.ac.jp(HC)

# Mathematical Models

A model developed by Baxter and Jain[1–4] is used to study the molecular transport in bone marrow (BM) using a spherical spatial domain that is consistent with imaging practices. We assume that the BM environment is homogeneous for consistent investigation into the overall interstitial fluid transport. Figure S6 illustrates this model along with a simplified model that is presented in the Maximum Pore Size Parameter Estimation section below. A bolus injection is applied and a continuous distributed source of macromolecules within the transvascular fluid from the vasculature is assigned to the entire spatial domain. All model parameter values used in this study can be found in Tables S1 and S2.

## Interstitial Fluid Pressure

In the interstitial space, we assume the fluid flow is axisymmetric and follows Darcy's law:

$$\mathbf{u} = -K\nabla p \tag{1}$$

where $\mathbf{u}$ is the interstitial fluid flow velocity (cm/s), $K$ is the hydraulic conductivity in the interstitial space of BM (cm$^2$/mm Hg-s), and $p$ is the interstitial fluid pressure (IFP, mm Hg). In this work, we estimate the hydraulic conductivity based on estimates made for cortical bone by Keanini et al.[5] and matching BM IFP measurements reported by Iversen et al.[6] The resulting value for $K$ is the same order-of-magnitude reported[5] and results in IFP profiles consistent with Iversen et al.[6]

We combine the continuity equation ($\nabla \cdot \mathbf{u} = \phi_v$) and Darcy's law (1) to obtain the steady-state fluid flow transport model:

$$-\nabla \cdot K\nabla p = \phi_v = L_p\frac{S}{V}(p_v - p - \sigma_T(\pi_v - \pi))$$

where $L_p$ is the hydraulic conductivity of the vascular walls (cm/mm Hg-s), $S$ is the vascular surface area (cm$^2$) and $V$ is the tissue volume (cm$^3$), $p_v$ is the vascular pressure (mm Hg), $\sigma_T$ is the osmotic reflection coefficient, $\pi_v$ is the osmotic pressure of the vascular fluid (mm Hg), and $\pi$ is the osmotic pressure of the interstitial fluid (mm Hg). The osmotic pressure term $\sigma_T(\pi_v - \pi)$ is small and can be neglected,[7] which simplifies the model to:

$$\nabla^2 p = \frac{L_p \rho_v}{K}(p - p_{ss})$$

where $p_{ss}$ is the steady-state IFP (mm Hg) which is equal to $p_v - \sigma_T(\pi_v - \pi)$ where the net efflux from the vessels is zero, and we have adopted the notation $\rho_v = S/V$ for the *vascular surface-to-volume ratio* (cm$^{-1}$). We define $r$ as the position (cm) from the center of the BM domain based on spherical coordinates for consistency with the experimental imaging procedures. At the center of the spherical domain, the fluid flow conforms to the no-flux condition, $\nabla p|_{r=0} = 0$, from axial symmetry. At the edge of the BM domain, we assume the IFP is equal to the surrounding pressure $p(r = R) = p_\infty$.

In this work, we have directly calculated an average $\rho_v$ from the experimental data. This was done as follows. From the individual images, the vascular surface area $S$ and vascular volume $V_v$ were estimated for both sinusoid and non-sinusoid vessels using an in-house algorithm[8,9] that skeletonizes the imaged vessels and measures the diameter $d_{v,i}$ and length $l_{v,i}$ of each vessel $i$. Assuming a cylindrical shape, the vascular volume is calculated as

$$V_v = \sum_{i=1}^{n_v} \frac{\pi l_{v,i} d_{v,i}^2}{4},$$

where $n_v$ is the total number of vessels. Correspondingly, the surface area of a cylinder is the derivative of its volume with respect to its radius $d_{v,i}/2$. Thus, we get

$$S = \sum_{i=1}^{n_v} \frac{4\pi l_{v,i} d_{v,i}}{4} = \sum_{i=1}^{n_v} \pi l_{v,i} d_{v,i}.$$

Nombela-Arrieta and Manz[10] reported that the blood in the BM of mice represents 15-30%

of the total tissue volume. We assume for the purposes of this work, that the blood in the BM is entirely contained in the vasculature (i.e., the volume of blood is equal to the vascular volume measured). A vascular surface-to-volume ratio was calculated for each mouse by taking the ratio of the total vascular surface area (both sinusoid and non-sinusoid), divided by the total vascular volume (both sinusoid and non-sinusoid) and multiplied by the median blood-to-tissue volume fraction[10] of 0.225. The individual surface-to-volume ratios were then averaged. The resulting experimentally measured average value was calculated to be $\rho_v$ =114.4 cm$^{-1}$ with a standard error of 48.6 cm$^{-1}$.

## Interstitial Transport

Macromolecule transport in the BM interstitial space can be both convective and diffusive as:

$$\frac{\partial C}{\partial t} + \nabla \cdot (\mathbf{u}C) = \nabla \cdot (D \nabla C) + \phi_s \tag{2}$$

where $C$ is the macromolecule concentration in the BM interstitium (g/ml),and $D$ is the diffusion coefficient (cm$^2$/s). The interstitial macromolecule concentration conforms to the no-flux condition at the center of the domain:

$$-D \left. \frac{\partial C}{\partial r} \right|_{r=0} + uC(r=0) = 0$$

and to the continuous boundary condition across the domain periphery, which is equal to $C(r = R) = C_\infty$. The source term $\phi_s$ is governed by the vascular system, and is discussed in the next section.

## Transvascular Flux (Pore Theory)

Based on the pore theory developed by Deen[17] and Bungay and Brenner[18], the transvascular hydraulic conductivity $L_p$, the vascular permeability $P$ (cm/s), and the solute reflection

Table S1: Physiological parameter values for the model used in this study are presented in this table.

| Parameter | Definition | Value | Reference |
|---|---|---|---|
| $K$ | Interstitial hydraulic conductivity [cm$^2$/mm Hg-s] | 2e-6 | This study |
| $\mu$ | Bone marrow fluid viscosity [mm Hg-s] | 1.25e-5 | 5,11 |
| $\rho_v$ | Vascular surface-to-volume ratio [cm$^{-1}$] | 114.4 | This study |
| $p_v$ | Vascular pressure [mm Hg] | 25 | 12 |
| $L$ | Vessel wall thickness [cm] | 5e-4 | 13 |
| $\gamma$ | Pore area fraction of vessel wall [-] | 1e-3 | 14 |

Table S2: Diffusion coefficients[15] and macromolecule half-life circulation time[16] are presented in this table. Half-life circulation times are calculated from a linear regression of the data reported by Kellaway et al.[16]

| Macromolecule Size [nm] | 4 | 8 | 13 | 32 |
|---|---|---|---|---|
| $D$ [cm$^2$/s] | 1.509e-6 | 8.545e-7 | 1.969e-7 | 1.375e-7 |
| $k_d$ [s] | 1689 | 9100 | 2236 | 6152 |

coefficient $\sigma$ are respectively given by

$$L_p = \frac{\gamma r_0^2}{8\mu L} \tag{3}$$

$$P = \frac{\gamma H D_0}{L} \tag{4}$$

$$\sigma = 1 - W$$

where $\gamma$ is the fraction of the vascular surface area occupied by pores, $r_0$ is the effective pore radius (cm), $\mu$ is the viscosity (mm Hg-s) of fluid in the pores assumed to be equivalent to the BM plasma viscosity, $L$ is the thickness of the vascular wall (cm), and $D_0$ is the diffusion coefficient of the macromolecule in free solution at 37°C given by the Stokes-Einstein relationship:

$$D_0 = \frac{k_B T}{6\pi\mu r_p}$$

where $k_B$ is Boltzmann's constant, $T$ is the absolute temperature, and $r_p$ is the radius of the diffusing macromolecule. In this study, we estimate $\mu$ as the average of the values reported by Keanini et al.[5] (2e-3 kg $\mathrm{m^{-1}s^{-1}}$) and that reported by Windberger et al.[11] (1.31e-3 kg $\mathrm{m^{-1}s^{-1}}$).

The diffusive hindrance factor $H$ and the convective hindrance factor $W$ are provided by Bungay and Brenner[18] as:

$$
\begin{aligned}
H &= \frac{6\pi\Phi}{K_t} \\
W &= \frac{\Phi(2-\Phi)K_s}{2K_t}
\end{aligned}
$$

with the partition coefficient as $\Phi = (1-\lambda)^2$ and $\lambda = r_p/r_0$ as the ratio of the diffusing macromolecule radius to pore radius. The $K_t$ and $K_s$ factors are defined as:[17,18]

$$
\begin{aligned}
K_t &= \frac{9}{4}\pi^2\sqrt{2}(1-\lambda)^{-5/2}\left[1+\sum_{k=1}^{2} a_k(1-\lambda)^k\right] + \sum_{k=0}^{4} a_{k+3}\lambda^k \\
K_s &= \frac{9}{4}\pi^2\sqrt{2}(1-\lambda)^{-5/2}\left[1+\sum_{k=1}^{2} b_k(1-\lambda)^k\right] + \sum_{k=0}^{4} b_{k+3}\lambda^k
\end{aligned}
$$

where the values of $a_k$ and $b_k$ are listed in Table S3.

Table S3: Hydrodynamic coefficients for the cylindrical pore model are presented in this table.

| $k$ | 1 | 2 | 3 | 4 | 5 | 6 | 7 |
|---|---|---|---|---|---|---|---|
| $a_k$ | -73/60 | 77293/50400 | -22.5083 | -5.6117 | -0.3363 | -1.216 | 1.647 |
| $b_k$ | 7/60 | -2227/50400 | 4.0180 | -3.9788 | -1.9215 | 4.392 | 5.006 |

On the short time scale, the binding between the macromolecules and cells, the extracellular components, and cellular uptake can be assumed negligible.[1] The continuous distributed source term $\phi_s$ (for the transport model (2)) is given by:

$$\begin{aligned}\phi_s &= L_p\rho_v(p_v - p)(1-\sigma)C_v + P\rho_v(C_v - C)\frac{Pe}{e^{Pe}-1} \\ &= L_p\rho_v(p_v - p)(1-\sigma)\frac{C_v e^{Pe} - C}{e^{Pe}-1},\end{aligned}$$

where $C_v$ is the concentration of the macromolecules in the blood vessels (g/ml), and we have introduced the Péclet number

$$Pe = L_p(p_v - p)(1-\sigma)/P, \tag{5}$$

which is defined as the ratio of convective to diffusive flux terms for transvascular transport. Based on the bolus injection model, the circulating macromolecule concentration follows a time-dependent exponential decay, $C_v = C_o e^{-t/k_d}$. $C_0$ is the initial macromolecule concentration, and $k_d$ is the macromolecules' circulation half-life.

# Effective Pore Size Parameter Estimation

To quantify the effective pore size (diameter) from the experimental data, we formulated and solved a parameter estimation problem that fits the model-predicted (simulated) transport phenomena to the experimental data. We assumed the interstitial hydraulic conductivity $K$ was fixed and only considered estimating the vascular hydraulic conductivity $L_p$ which is a function of the vessel pore radius $r_0$ as the only free variable (from (3) above). From (3), we derived an expression for $r_0$ as a function of $L_p$

$$r_0 = \sqrt{\frac{8L_p\mu L}{\gamma}} \tag{6}$$

and substituted this expression into every term in the pore theory model. All other physiological parameters are considered constant with the values shown in Table S1 and Table S2.

As a result, the pore theory model equations were all explicit functions of $L_p$. The parameter estimation problem utilizes the sum-of-squared errors (SSE) objective, and is formulated as:

$$\min_{x \in X} \sum_{i=1}^{n} \left( C_{\text{avg}}^{\text{model}}(t_i, x) - C_{\text{avg}}^{\text{data}}(t_i) \right)^2 \tag{7}$$

where $x$ is the uncertain physiological parameter taken as the vascular hydraulic conductivity $L_p$, and $n$ is the total number of discrete time points considered for fitting the data.

To simulate the spatiotemporal concentration profiles $C$, we nondimensionalize the variables in the transport model with centered finite differencing and upwind differencing to discretize the fluid transport model and the macromolecule transport model, respectively. First, we solve the fluid transport model to obtain the IFP profile over the BM domain. The velocity profile is derived from Darcy's law (1). Then, within the optimization problem, a variable stepsize $4^{\text{th}}$-order Runge-Kutta method is used to solve the transient convection-diffusion macromolecule transport model (2) to obtain the interstitial macromolecule concentration profile $C$. We average the macromolecule concentration over the spatial domain and take it as a model prediction $C_{\text{avg}}^{\text{model}}$ for the parameter estimation problem.

The experimental average macromolecule concentration $C_{\text{avg}}^{\text{data}}$, was derived by the same methodology as the transport model using a spatial average macromolecule balance, written as:

$$\frac{dC_{\text{avg}}^{\text{data}}}{dt} = P_{\text{eff}} \rho_v (C_v - C_{\text{avg}}^{\text{data}}). \tag{8}$$

The effective permeability $P_{\text{eff}}$ was quantified from the experimentally observed flux across the vascular wall, which includes both convective and diffusive transvascular terms but may overestimate the diffusive components.[1]

To solve the optimization problem (7), we deploy the interior-point solver within `fmincon` in MATLAB (The Mathworks). To improve the solution estimates, a multistart approach was used which automatically generates initial guesses for fmincon. Local optimal solutions are returned, and the "best-found" solution is reported. This approach does not guarantee global optimality and so a final analysis comparing the model to the experimental data was used to verify goodness of fit. From the optimal $L_p$ values obtained, the corresponding vessel pore radius $r_0$ is calculated using (6). The local optimization results for pore sizes within different experimental groups are contained in Table S4.

The experimental average macromolecule concentration $C_{\text{avg}}^{\text{data}}$ profiles are plotted with standard error for each macromolecule against the best-fit model prediction in Figures S2-S4. In each case, the model prediction falls within the standard error bounds for the experimental profiles and fits the data very well. For larger measured effective permeabilities ($\gtrsim$ 2e-6 cm/s), there is some structural mismatch observed in the form of bias in the model prediction. This is most significantly pronounced in the 10 kDa (4 nm) dextran results (see Fig. 2(a)-2(b)). In this case, the effective permeability measurement significantly overestimates the contribution of diffusion to the total mass flux. Thus, the experimental average macromolecule concentration profiles given by (8) are less accurate for smaller macromolecules. Consequently, the parameter estimation results predict effective pore sizes that are much larger than expected.

Table S4: Optimization results for the optimal vessel pore size (in diameter as $2r_0^*$ (nm)) are summarized for each experiment group. The experimentally measured effective permeability $P_{\text{eff}}$ (cm/s) values and their corresponding standard error (STE) (cm/s) are included.

| **6 Mouse Group** | | | | | | |
|---|---|---|---|---|---|---|
| | 10 kDa (4 nm) dextran | | | 70 kDa (13 nm) dextran | | |
| | $P_{\text{eff}}$ | STE | Pore Size | $P_{\text{eff}}$ | STE | Pore Size |
| Sinusoid | 6.0435e-6 | 1.3650e-6 | 216.35 | 2.8685e-6 | 1.4913e-6 | 98.61 |
| Non-sinusoid | 4.2846e-6 | 1.8639e-6 | 135.04 | 1.2457e-6 | 2.6192e-7 | 48.45 |
| **5 Mouse Group** | | | | | | |
| | 70 kDa (13 nm) dextran | | | 500 kDa (32 nm) dextran | | |
| | $P_{\text{eff}}$ | STE | Pore Size | $P_{\text{eff}}$ | STE | Pore Size |
| Sinusoid | 1.1343e-6 | 2.6317e-7 | 46.13 | 5.0977e-7 | 7.2433e-8 | 55.97 |
| Non-sinusoid | 7.0457e-7 | 1.9649e-7 | 36.81 | 3.2536e-7 | 9.9688e-8 | 50.49 |
| **8 Mouse Group** | | | | | | |
| | 70 kDa (13 nm) dextran | | | BSA (8 nm) | | |
| | $P_{\text{eff}}$ | STE | Pore Size | $P_{\text{eff}}$ | STE | Pore Size |
| Sinusoid | 1.4217e-6 | 3.0583e-7 | 52.58 | 9.3025e-7 | 2.8044e-7 | 37.58 |
| Non-sinusoid | 7.4697e-7 | 8.3522e-8 | 35.75 | 4.2075e-7 | 9.3642e-8 | 24.57 |

# Maximum Pore Size Parameter Estimation

To estimate the maximum vessel pore size, we ignored interstitial transport and continuity, and considered only the transvascular flux (pore theory) model using the assumption that $P/P_{\text{eff}} \leq 0.10$ (i.e., the diffusive contribution to total flux is less than 10%) from Baxter and Jain.[1] By calculating the Péclet number for transvascular flux, we estimate the relative contribution of convective to diffusive mass transport across the vascular wall. We formulated the model-predicted effective permeability as

$$P_{\text{eff}}^{\text{model}} = P(1 + Pe) \tag{9}$$

where $P$ is given by (4) and $Pe$ is given by (5). To estimate the vessel pore size, the following parameter estimation problem was formulated and solved:

$$\min_{r_0} \chi^2 = \frac{1}{n} \sum_{i=1}^{n} \left( P_{\text{eff}}^{\text{exp},i} - P_{\text{eff}}^{\text{model}} \right)^2 \tag{10}$$

where $P_{\text{eff}}^{\text{exp},i}$ represents the $i^{\text{th}}$ experimentally measured effective permeability for a given macromolecule hydrodynamic diameter in an experimental group and $n$ is the number of measurements made for that experimental group. An illustration of this simplified model for estimating the maximum pore size is provided in Figure S6.

In this study, we used the data from the 500 kDa dextran (32 nm) experiments and varied the quantity $1 + Pe$ between 10 and 500, representing $P/P_{\text{eff}}$ values between 0.002 and 0.10. The results are plotted in Figure S5. As expected, systems with greater diffusive transport contributions to total flux (smaller $Pe$) require larger effective pore sizes to yield the experimentally measured $P_{\text{eff}}$ values. This is consistent with our previous results for the 4 nm dextran overestimating the diffusive mass transport contribution resulting in much larger than expected effective pore sizes. To estimate the maximum pore size for each vessel type, we used the smallest $Pe$ values predicted by the optimally fit transport model (2); $Pe \approx 91.6$ for sinusoid and $Pe \approx 136.2$ for non-sinusoid vessels. We then solved (10) to guaranteed global optimality using the EAGO solver[19,20] version 0.3.1 via the JuMP modeling language[21] version 0.2.1 in the Julia programming language[22] version 1.4.1 to obtain maximum vessel pore sizes of 61 nm and 53 nm for sinusoid and non-sinusoid vessels, respectively. An illustration is provided in Figure S7 of a vessel wall with a distribution of pore cutoff sizes up to the estimated maximum that was determined by this simplified model, depicting the effects on the transvascular flux of macromolecules.

## Supplementary Figures

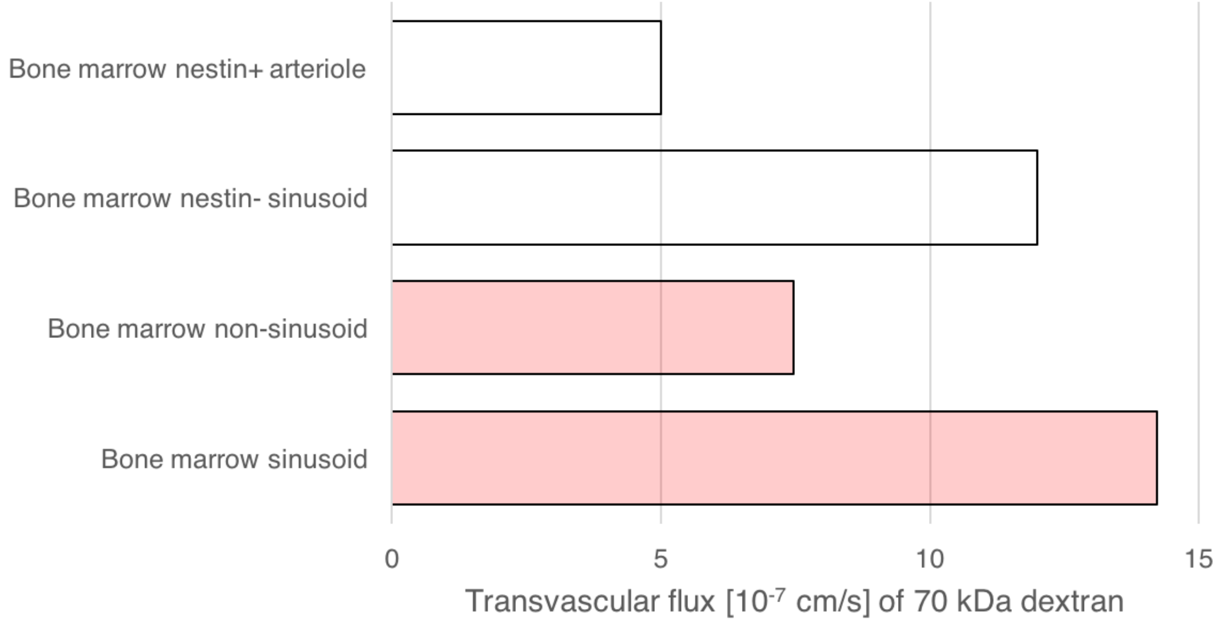

Figure S1: Effective permeability of bone marrow sinusoids and non-sinusoids to 70 kDa dextrans. Permeability of BM sinusoids and non-sinusoids to 70 kDa dextrans are comparable whether identified by nestin[23] (white bars) or morphology as in the current study (red bars).

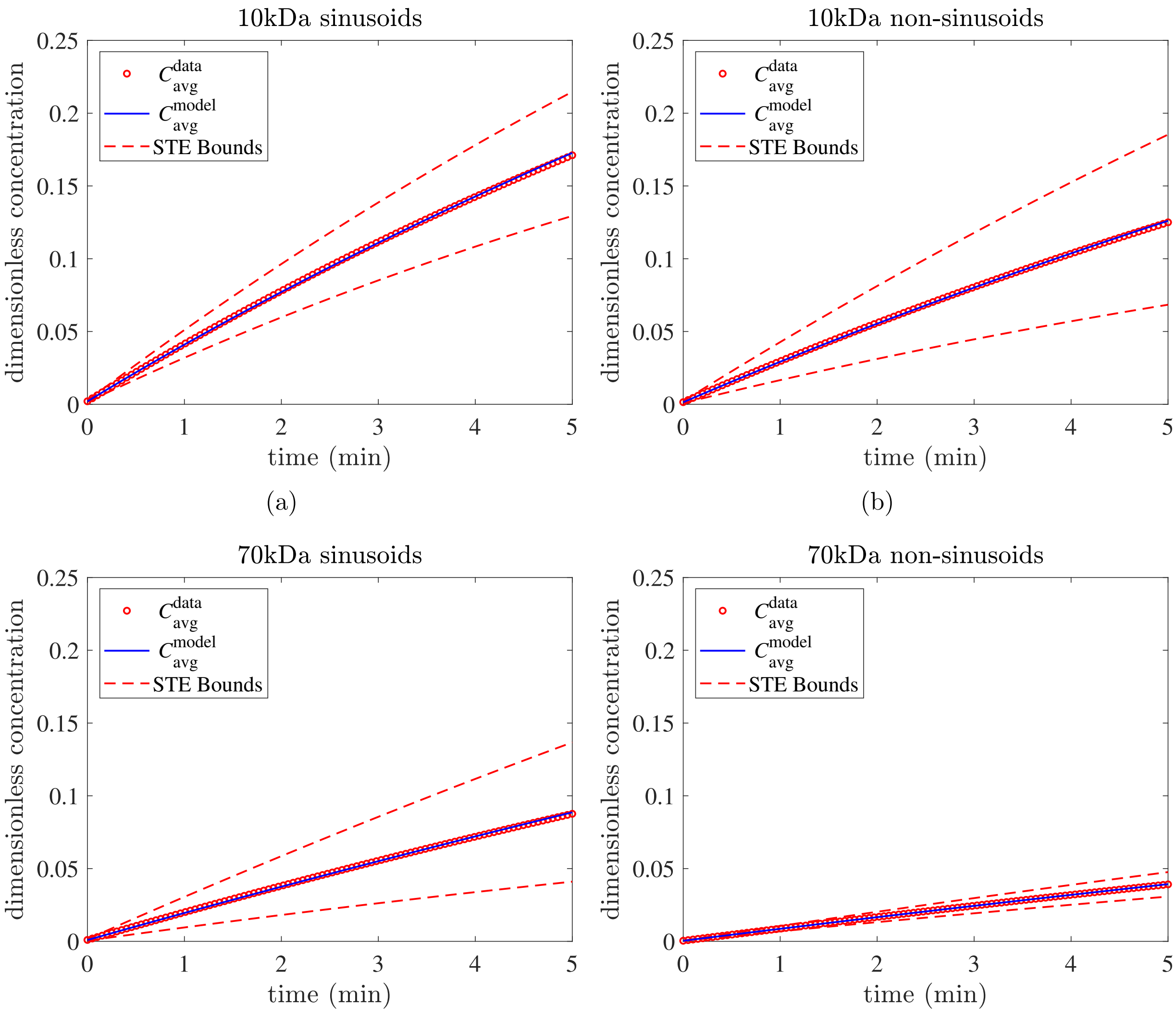

(a) (b) (c) (d)

Figure S2: The experimental data and optimal model predictions from the parameter estimation problem (7) are plotted for the 6-mouse group. Top row: 10 kDa (4 nm) dextran in (a) sinusoid and (b) non-sinusoid vessels. Bottom row: 70kDa (13 nm) dextran in (c) sinusoid and (d) non-sinusoid vessels. The solid lines are the average macromolecule concentration profiles $C_{\text{avg}}^{\text{model}}$ as predicted by the transport model with the optimal fit to the experimental average macromolecule concentration profile data $C_{\text{avg}}^{\text{data}}$ (open circles). Dashed lines are the standard error bounds on the experimental average macromolecule concentration profile as calculated from the standard error of the experimentally measured effective permeabilities.

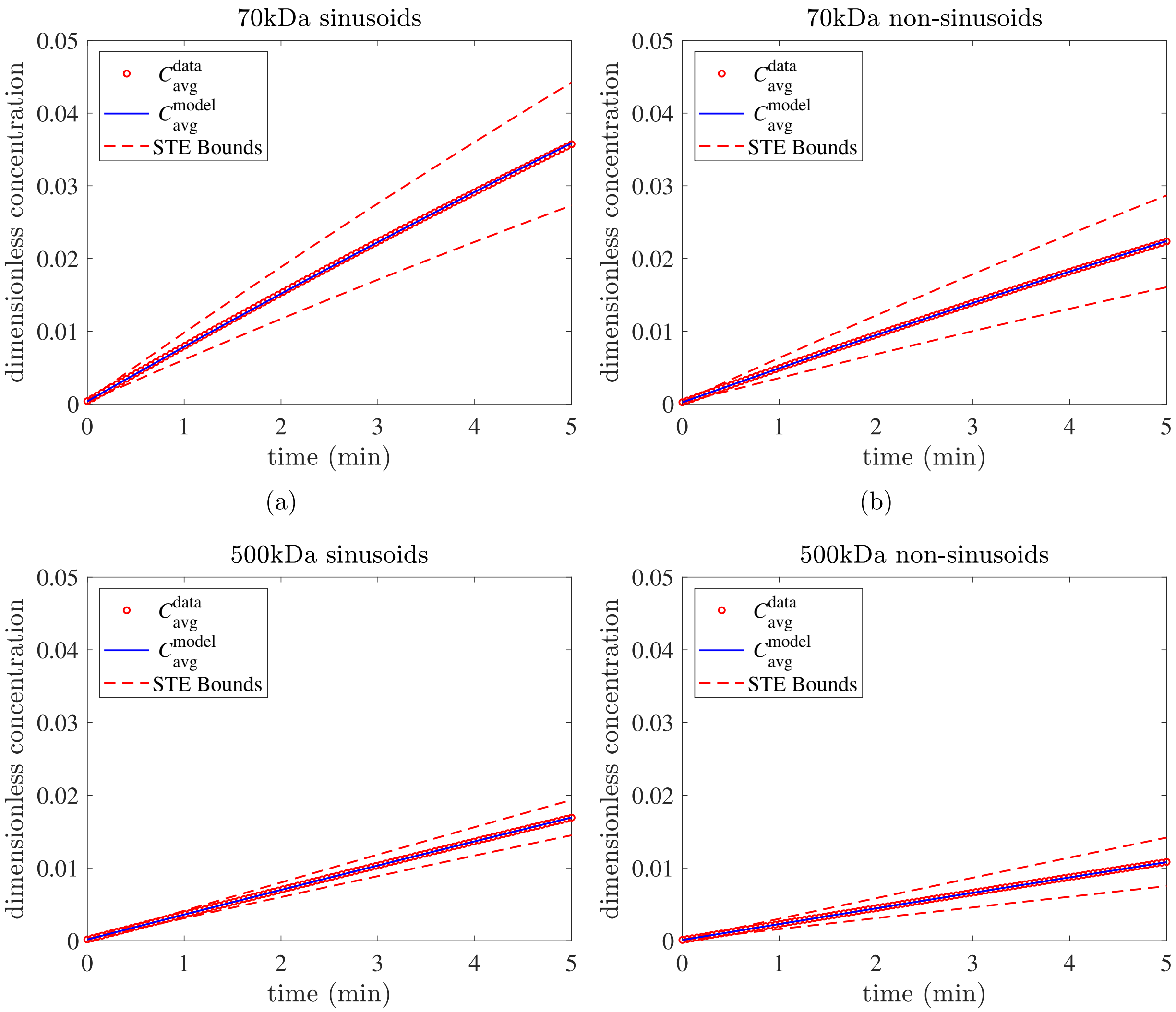

(a) (b) (c) (d)

Figure S3: The experimental data and optimal model predictions from the parameter estimation problem (7) are plotted for the 5-mouse group. Top row: 70 kDa (13 nm) dextran in (a) sinusoid and (b) non-sinusoid vessels. Bottom row: 500 kDa (32 nm) dextran in (c) sinusoid and (d) non-sinusoid vessels. The solid lines are the average macromolecule concentration profiles $C_{\text{avg}}^{\text{model}}$ as predicted by the transport model with the optimal fit to the experimental average macromolecule concentration profile data $C_{\text{avg}}^{\text{data}}$ (open circles). Dashed lines are the standard error bounds on the experimental average macromolecule concentration profile as calculated from the standard error of the experimentally measured effective permeabilities.

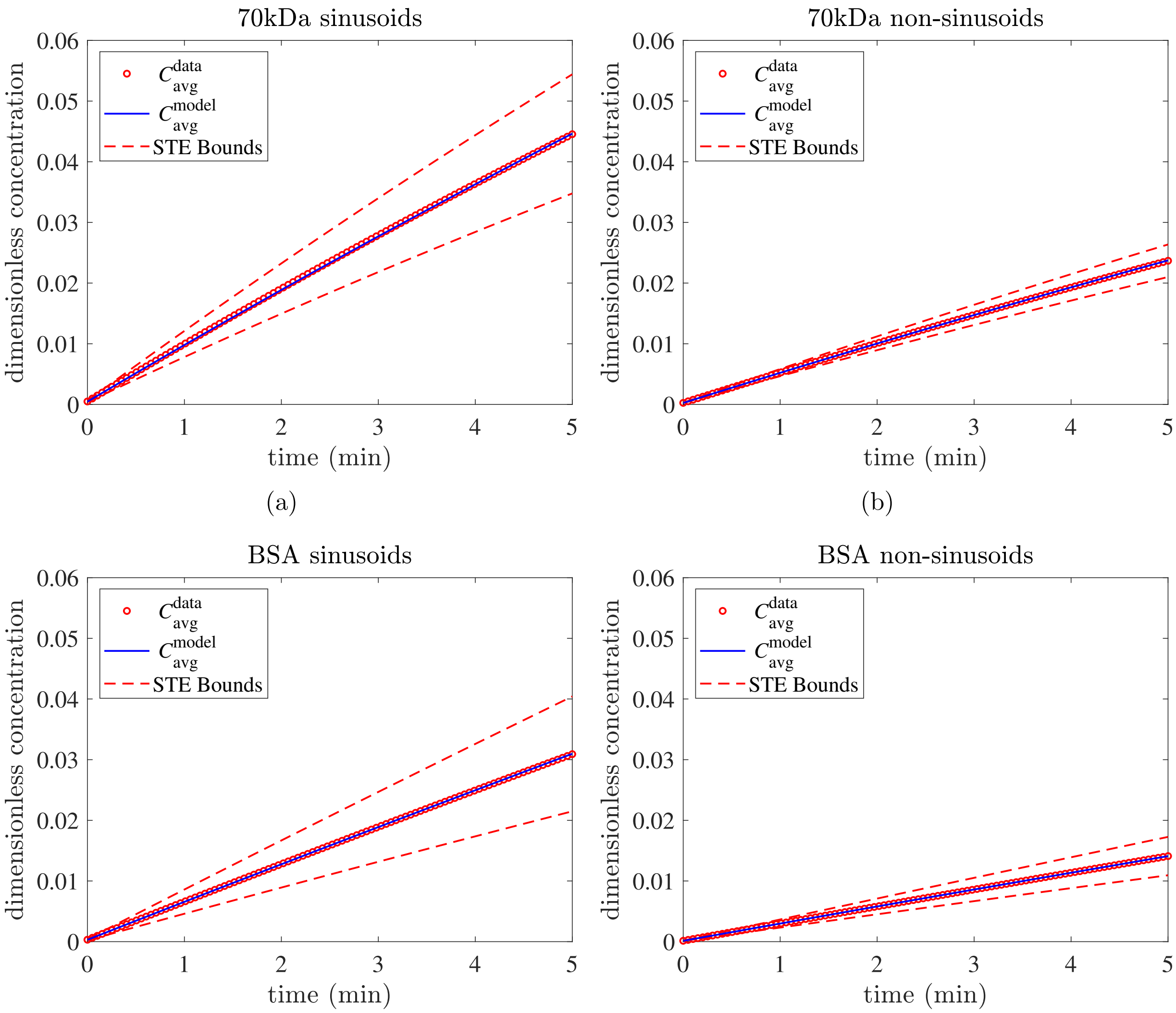

(a) (b)

(c) (d)

Figure S4: The experimental data and optimal model predictions from the parameter estimation problem (7) are plotted for the 8-mouse group. Top row: 70 kDa (13 nm) dextran in (a) sinusoid and (b) non-sinusoid vessels. Bottom row: BSA (8 nm) in (c) sinusoid and (d) non-sinusoid vessels. The solid lines are the average macromolecule concentration profiles $C_{\text{avg}}^{\text{model}}$ as predicted by the transport model with the optimal fit to the experimental average macromolecule concentration profile data $C_{\text{avg}}^{\text{data}}$ (open circles). Dashed lines are the standard error bounds on the experimental average macromolecule concentration profile as calculated from the standard error of the experimentally measured effective permeabilities.

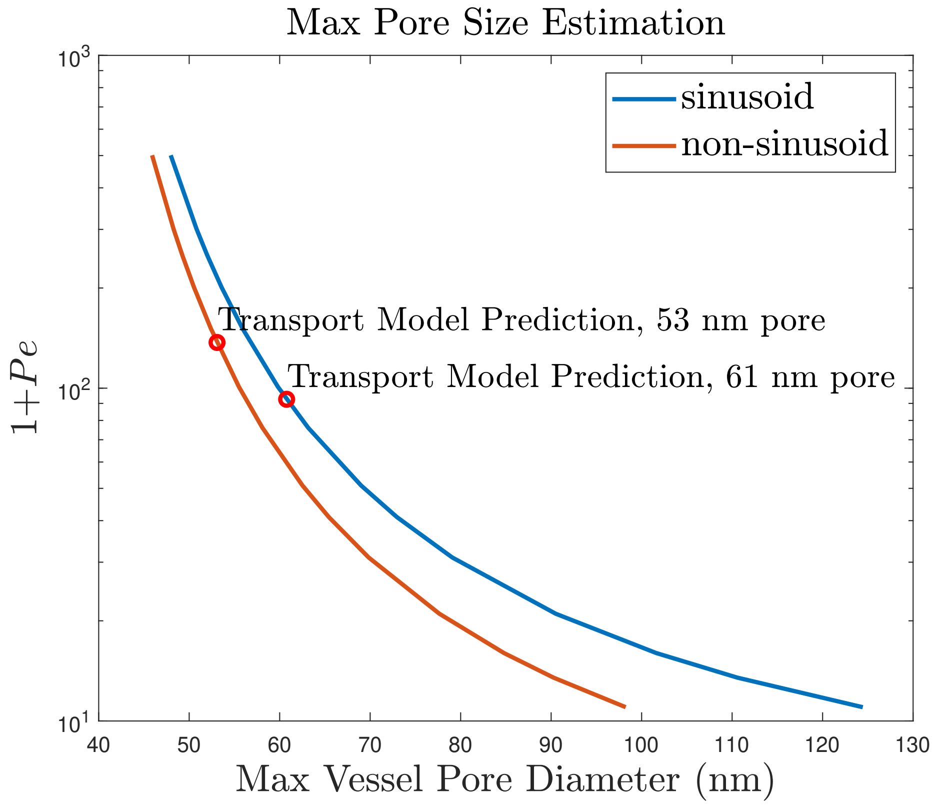

Figure S5: The estimated maximum vessel pore sizes (diameter in nm) versus the Péclet number illustrates the sensitivity of the pore size as predicted by the pore theory model to the relative contributions of diffusive and convective transport. These profiles pertain to the 500 kDa (32 nm) dextran for both sinusoid and non-sinusoid vessels. The transport model-predicted $Pe$ values are plotted against the estimated maximum pore sizes (open circles) for each vessel type.

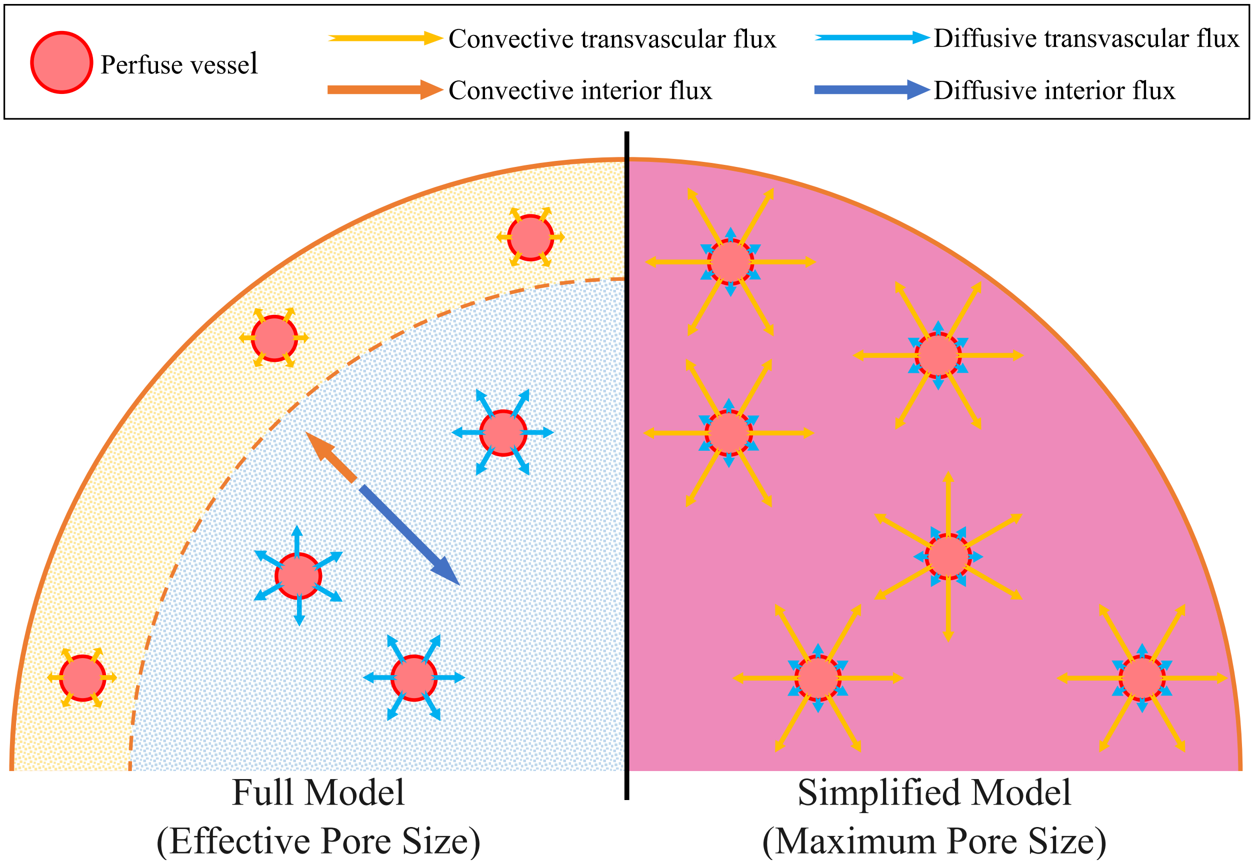

Figure S6: A cross-section of the spherical bone marrow tissue volume is illustrated with respect to the two mathematical models considered in this work. The arrows indicate the direction and relative contribution of each mode of mass transport. (Left) The full model used to estimate the effective pore sizes (Effective Pore Size Parameter Estimation section) accounts for both convective and diffusive transvascular flux and interior/interstitial flux. In the yellow region on the rim, interstitial and transvascular convective transport dominates flux (perfused vessels and yellow arrows). In the interior light blue region, interstitial and transvascular diffusive transport dominates flux (perfused vessels and light blue arrows). Due to fluid pressure and concentration gradients, respectively, net convective transport goes out radially (orange arrow), but it is less than net diffusive transport (longer dark blue arrow), which goes in radially. (Right) The simplified model used to estimate the maximum pore sizes (Maximum Pore Size Parameter Estimation section) ignores transport in the interior of the bone marrow tissue and only considers transvascular flux; indicated by a lack of background texture. In this model, we focus on higher Péclet numbers for transvascular flux with diffusive flux contributing $< 10\%$ to the total flux depicted by relative arrow lengths.

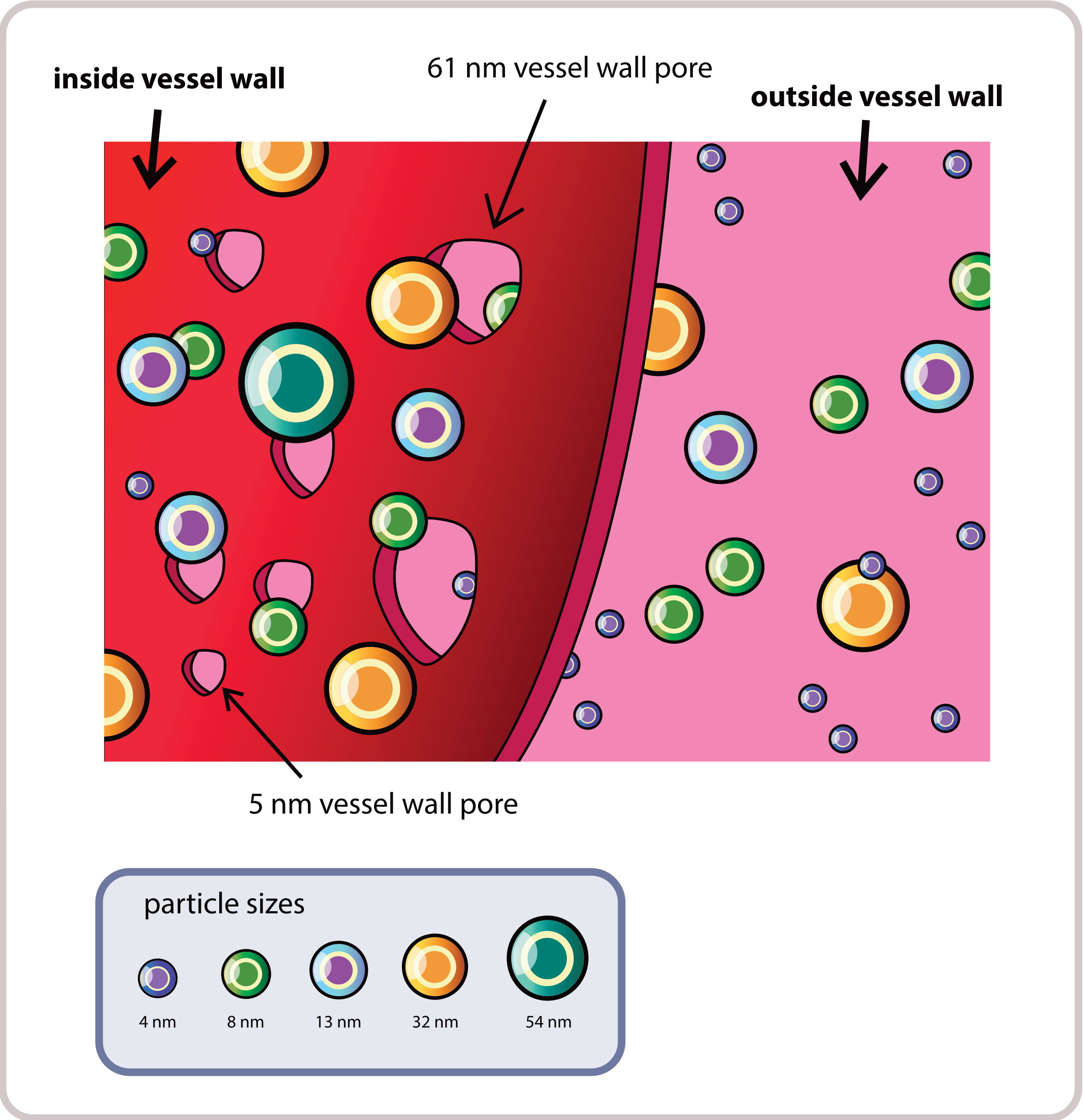

Figure S7: The models depicted in Figure S6 were used to predict the effective and maximum pore sizes of murine sinusoids and non-sinusoids in the bone marrow from measurements of transvascular flux. On the left, the interior of a vessel is depicted, while the extravascular space outside of the vessel wall is depicted on the right. On the wall, there is a distribution of sizes of pores, from the 5 nm that was previously thought to be the pore cutoff size of bone marrow vessels to 61nm, which we predict is the pore cutoff size of non-sinusoidal murine bone marrow vessels. A range of particles with various hydrodynamic diameters are depicted to represent the dextrans (4 nm, 13 nm, 32 nm, 54 nm) and bovine serum albumin (8 nm). Notice that a greater fraction of smaller particles can extravasate from inside the vessel wall after intravenous injection, while the 54 nm particle in particular is limited from crossing due to its hydrodynamic diameter approaching the maximum pore cutoff size.

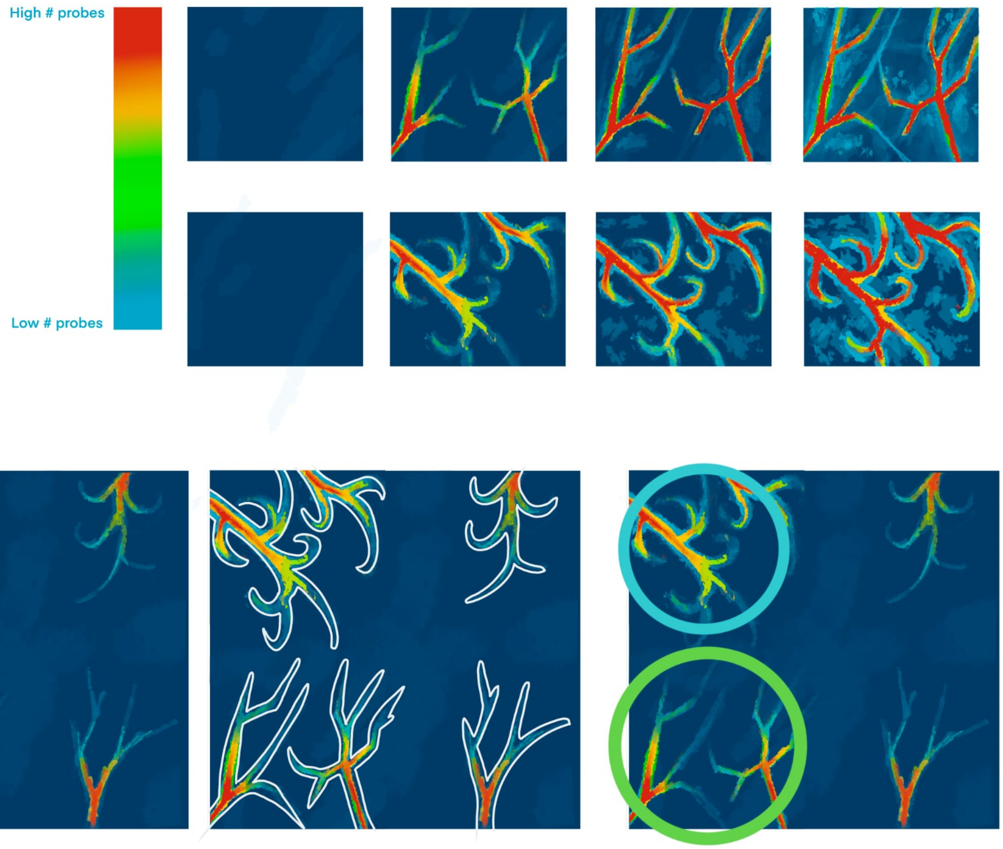

Figure S8: A schematic of the image analysis process. Images of fluorescent signal (depicted with a high low look up table) were collected continuously over a 10-minute period (top row) from immediately before injection of probes (upper left panels). Immediately after injection, the image collected was considered vascular contrast (bottom left panel) and a custom MATLAB code segmented vessels automatically using fluorescent intensity- and size-thresholding (bottom middle panel). After segmenting, a researcher manually selected regions of sinusoids (bottom right, light blue area) from regions of non-sinusoids (bottom right, green area) based on vascular morphology.

# Supplementary Tables

Table S5: In pivotal clinical trials of approved nanocarriers, encapsulation of small molecules reduces hematological toxicity compared to small-molecule chemotherapy administration, but the loaded nanocarriers introduce hematological toxicity compared to no treatment. The table contents were selected and updated from Chauhan et al.[24] and Martin et al.[25]

[a] Drug delivery system (DDS).

[b] Control drug regimen of small molecules.

[c] Effect on hematological toxicity (Grade 3 or 4 neutropenia).

| Nanocarrier (regimen) | Cancer | DDS[a] Diameter [nm] | Control Drug[b] | Effect[c] |
|---|---|---|---|---|
| Liposomal doxorubicin (monotherapy) | Breast | 80[16] | Doxorubicin | Decreased<br>(from 4% to 1% of patients)[26] |
| Albumin-bound paclitaxel (monotherapy) | Breast | 10[14] | Paclitaxel | Decreased<br>(from ∼45% to ∼30% of patients)[27] |
| Albumin-bound paclitaxel (gemcitabine) | Pancreas | 10[14] | Gemcitabine | Increased<br>(from 27% to 38% of patients)[28] |
| Liposomal irinotecan (fluorouracil and folinic acid) | Pancreas | 90 | Fluorouracil and folinic acid | Increased<br>(from 1% to 27% of patients)[29] |

Table S6: The properties of each injected macromolecule are presented in this table. The data is provided by the manufacturer unless otherwise noted.

| Macromolecule (Manufacturer) | Molecular Weight [kDa] | Hydrodynamic Diameter [nm] | Polydispersity Index | Fluorescent Dye | Labeling |
|---|---|---|---|---|---|
| Dextran (Sigma-Aldrich) | 10 | ∼4[30] | 0.3[31] | FITC | 0.003–0.002 mol FITC per mol glucose |
| Dextran (Sigma-Aldrich) | 70 | ∼13[30] | 0.15[31] | RITC | 0.002–0.015 mol RITC per mol glucose |
| Dextran (Sigma-Aldrich) | 500 | ∼32[30] | - | FITC | 0.01 mol/mol FITC glucose |
| Dextran (Sigma-Aldrich) | 2000 | ∼54[30] | 0.55[31] | FITC | 0.003–0.020 mol FITC per mol glucose |
| BSA (Sigma-Aldrich) | 66 | 8[30] | - | FITC | ≥7 mol FITC per mol albumin |
| Polymeric micelle (lab made) | - | 30[32] | 0.16[32] | Alexa 488 | - |
| Polymeric micelle (lab made) | - | 69[32] | 0.12[32] | Alexa 647 | - |

Table S7: The parameters for each experiment are tabulated.
[a] Phosphate buffered saline (PBS).

| Experiment | Figure | Probe 1 | Probe 2 | Imaging Time |
|---|---|---|---|---|
| Qualitative extravasation of 10 kDa dextran | 1B | FITC 2,000 kDa dextran (0.01 mg dextran in 20 $\mu$l PBS[a]) | FITC 10 kDa dextran (100 $\mu$l of 2 mg/kg dextran) | 2 min starting when Probe 1 was administered followed by 10 min of imaging following administration of Probe 2 |
| Qualitative extravasation of 70 kDa dextran | 1C | RITC 70 kDa dextran (100 $\mu$l of 8 mg/kg dextran) | No probe | 10 min continuously starting immediately before co-injection, with another image at 80 min |
| Qualitative extravasation of 70 kDa dextran | 1D | RITC 70 kDa dextran (100 $\mu$l of 8 mg/kg dextran) | FITC 500 kDa dextran (100 $\mu$l of 2 mg/kg dextran) | 10 min continuously starting immediately before co-injection, with another image at 80 min |
| Quantitative sinusoid versus non-sinusoid | 2 | RITC 70 kDa dextran (100 $\mu$l of 8 mg/kg dextran) | Various but not presented (used data from any experiment with 70 kDa dextran) | 10 min continuously starting immediately before co-injection |
| Quantitative 70 kDa versus 10 kDa permeability | 3 | RITC 70 kDa dextran (100 $\mu$l of 8 mg/kg dextran) | FITC 10 kDa dextran (100 $\mu$l of 2 mg/kg dextran) | 10 min continuously starting immediately before co-injection |
| Quantitative 70 kDa versus BSA permeability | 4 | RITC 70 kDa dextran (100 $\mu$l of 8 mg/kg dextran) | FITC BSA (100 $\mu$l of 2 mg/kg dextran) | 10 min continuously starting immediately before co-injection |
| Quantitative 70 kDa versus 500 kDa permeability | 5 | RITC 70 kDa dextran (100 $\mu$l of 8 mg/kg dextran) | FITC 500 kDa dextran (100 $\mu$l of 2 mg/kg dextran) | 10 min continuously starting immediately before co-injection |
| Qualitative extravasation of 30 nm micelle versus 70 nm micelle | 6 | 30 nm micelle (10 mg/kg)[32] | 70 nm micelle (10 mg/kg)[32] | 10 min continuously starting immediately before co-injection |

# References

(1) Baxter, L. T.; Jain, R. K. Transport of fluid and macromolecules in tumors. I. Role of interstitial pressure and convection. *Microvascular Research* **1989**, *37*, 77–104.

(2) Baxter, L. T.; Jain, R. K. Transport of fluid and macromolecules in tumors. II. Role of heterogeneous perfusion and lymphatics. *Microvascular Research* **1990**, *40*, 246–263.

(3) Baxter, L. T.; Jain, R. K. Transport of fluid and macromolecules in tumors: III. Role of binding and metabolism. *Microvascular Research* **1991**, *41*, 5–23.

(4) Baxter, L. T.; Jain, R. K. Transport of fluid and macromolecules in tumors. IV. A microscopic model of the perivascular distribution. *Microvascular Research* **1991**, *41*, 252–272.

(5) Keanini, R. G.; Roer, R. D.; Dillaman, R. M. A theoretical model of circulatory interstitial fluid flow and species transport within porous cortical bone. *Journal of Biomechanics* **1995**, *28*, 901–914.

(6) Iversen, P. O.; Berggreen, E.; Nicolaysen, G.; Heyeraas, K. Regulation of extracellular volume and interstitial fluid pressure in rat bone marrow. *American Journal of Physiology-Heart and Circulatory Physiology* **2001**, *280*, H1807–H1813.

(7) Stohrer, M.; Boucher, Y.; Stangassinger, M.; Jain, R. Oncotic pressure in human tumor xenografts. Proceedings of the American Association of Cancer Research. 1995; p 311.

(8) Tyrrell, J.; Mahadevan, V.; Tong, R.; Brown, E.; Jain, R.; Roysam, B. A 2-D/3-D model-based method to quantify the complexity of microvasculature imaged by in vivo multiphoton microscopy. *Microvascular Research* **2005**, *70*, 165–178.

(9) Tyrrell, J.; Roysam, B.; di Tomaso, E.; Tong, R.; Brown, E.; Jain, R. Robust 3-D modeling of tumor microvasculature using superellipsoids. 3rd IEEE International Symposium on Biomedical Imaging: Nano to Macro, 2006. 2006; pp 185–188.

(10) Nombela-Arrieta, C.; Manz, M. G. Quantification and three-dimensional microanatomical organization of the bone marrow. *Blood Advances* **2017**, *1*, 407–416.

(11) Windberger, U.; Bartholovitsch, A.; Plasenzotti, R.; Korak, K.; Heinze, G. Whole blood viscosity, plasma viscosity and erythrocyte aggregation in nine mammalian species: reference values and comparison of data. *Experimental Physiology* **2003**, *88*, 431–440.

(12) Boucher, Y.; Jain, R. K. Microvascular pressure is the principal driving force for interstitial hypertension in solid tumors: implications for vascular collapse. *Cancer Research* **1992**, *52*, 5110–5114.

(13) Jain, R. K. Transport of molecules across tumor vasculature. *Cancer and Metastasis Reviews* **1987**, *6*, 559–593.

(14) Chauhan, V. P.; Stylianopoulos, T.; Martin, J. D.; Popovic, Z.; Chen, O.; Kamoun, W. S.; Bawendi, M. G.; Fukumura, D.; Jain, R. K. Normalization of tumour blood vessels improves the delivery of nanomedicines in a size-dependent manner. *Nature Nanotechnology* **2012**, *7*, 383–388.

(15) Pluen, A.; Boucher, Y.; Ramanujan, S.; McKee, T. D.; Gohongi, T.; di Tomaso, E.; Brown, E. B.; Izumi, Y.; Campbell, R. B.; Berk, D. A., et al. Role of tumor–host interactions in interstitial diffusion of macromolecules: cranial vs. subcutaneous tumors. *Proceedings of the National Academy of Sciences* **2001**, *98*, 4628–4633.

(16) Kellaway, I. W.; Seale, L.; Spencer, P. S. The in Vitro Characterization and Biostability of $^{99m}$Tc-Dextran and Its Accumulation Within the Inflamed Paws of Adjuvant-Induced Arthritic Rats. *Pharmaceutical Research* **1995**, *12*, 588–593.

(17) Deen, W. Hindered transport of large molecules in liquid-filled pores. *AIChE Journal* **1987**, *33*, 1409–1425.

(18) Bungay, P. M.; Brenner, H. The motion of a closely-fitting sphere in a fluid-filled tube. *International Journal of Multiphase Flow* **1973**, *1*, 25–56.

(19) Wilhelm, M. E.; Stuber, M. D. EAGO.jl: Easy Advanced Global Optimization in Julia. *Optimization Methods and Software* **2020**, 1–26.

(20) Wilhelm, M.; Stuber, M. D. EAGO: Easy Advanced Global Optimization Julia Package. 2018; `https://github.com/PSORLab/EAGO.jl`.

(21) Dunning, I.; Huchette, J.; Lubin, M. JuMP: A modeling language for mathematical optimization. *SIAM Review* **2017**, *59*, 295–320.

(22) Bezanson, J.; Edelman, A.; Karpinski, S.; Shah, V. B. Julia: A fresh approach to numerical computing. *SIAM Review* **2017**, *59*, 65–98.

(23) Itkin, T.; Gur-Cohen, S.; Spencer, J. A.; Schajnovitz, A.; Ramasamy, S. K.; Kusumbe, A. P.; Ledergor, G.; Jung, Y.; Milo, I.; Poulos, M. G., et al. Distinct bone marrow blood vessels differentially regulate haematopoiesis. *Nature* **2016**, *532*, 323–328.

(24) Chauhan, V. P.; Martin, J. D.; Liu, H.; Lacorre, D. A.; Jain, S. R.; Kozin, S. V.; Stylianopoulos, T.; Mousa, A. S.; Han, X.; Adstamongkonkul, P., et al. Angiotensin inhibition enhances drug delivery and potentiates chemotherapy by decompressing tumour blood vessels. *Nature Communications* **2013**, *4*, 2516.

(25) Martin, J. D.; Cabral, H.; Stylianopoulos, T.; Jain, R. K. Improving Cancer Immunotherapy Using Nanomedicines: Profess, Opportunities and Challenges. *Nature Reviews Clinical Oncology* **2020**, *17*, 251–266.

(26) O'Brien, M.; Wigler, N.; Inbar, M.; Rosso, R.; Grischke, E.; Santoro, A.; Catane, R.; Kieback, D.; Tomczak, P.; Ackland, S.; Orlandi, F.; Mellars, L.; Alland, L.; Tendler, C.

Reduced cardiotoxicity and comparable efficacy in a Phase III trial of pegylated liposomal doxorubicin HCl(CAELYX$^{\text{TM}}$/Doxil$^{®}$) versus conventional doxorubicin for first-line treatment of metastatic breast cancer. *Annals of Oncology* **2004**, *15*, 440–449.

(27) Gradishar, W. J.; Tjulandin, S.; Davidson, N.; Shaw, H.; Desai, N.; Bhar, P.; Hawkins, M.; O'Shaughnessy, J. Phase III Trial of Nanoparticle Albumin-Bound Paclitaxel Compared With Polyethylated Castor Oil–Based Paclitaxel in Women With Breast Cancer. *Journal of Clinical Oncology* **2005**, *23*, 7794–7803.

(28) Von Hoff, D. D.; Ervin, T.; Arena, F. P.; Chiorean, E. G.; Infante, J.; Moore, M.; Seay, T.; Tjulandin, S. A.; Ma, W. W.; Saleh, M. N.; Harris, M.; Reni, M.; Dowden, S.; Laheru, D.; Bahary, N.; Ramanathan, R. K.; Tabernero, J.; Hidalgo, M.; Goldstein, D.; Van Cutsem, E.; Wei, X.; Iglesias, J.; Renschler, M. F. Increased Survival in Pancreatic Cancer with nab-Paclitaxel plus Gemcitabine. *New England Journal of Medicine* **2013**, *369*, 1691–1703.

(29) Wang-Gillam, A.; Li, C.-P.; Bodoky, G.; Dean, A.; Shan, Y.-S.; Jameson, G.; Macarulla, T.; Lee, K.-H.; Cunningham, D.; Blanc, J. F.; Hubner, R. A.; Chiu, C.-F.; Schwartsmann, G.; Siveke, J. T.; Braiteh, F.; Moyo, V.; Belanger, B.; Dhindsa, N.; Bayever, E.; Von Hoff, D. D.; Chen, L.-T.; Adoo, C.; Anderson, T.; Asselah, J.; Azambuja, A.; Bampton, C.; Barrios, C. H.; Bekaii-Saab, T.; Bohuslav, M.; Chang, D.; Chen, J.-S.; Chen, Y.-C.; Choi, H. J.; Chung, I. J.; Chung, V.; Csoszi, T.; Cubillo, A.; DeMarco, L.; de Wit, M.; Dragovich, T.; Edenfield, W.; Fein, L. E.; Franke, F.; Fuchs, M.; Gonzales-Cruz, V.; Gozza, A.; Fernando, R. H.; Iaffaioli, R.; Jakesova, J.; Kahan, Z.; Karimi, M.; Kim, J. S.; Korbenfeld, E.; Lang, I.; Lee, F.-C.; Lee, K.-D.; Lipton, L.; Ma, W. W.; Mangel, L.; Mena, R.; Palmer, D.; Pant, S.; Park, J. O.; Piacentini, P.; Pelzer, U.; Plazas, J. G.; Prasad, C.; Rau, K.-M.; Raoul, J.-L.; Richards, D.; Ross, P.; Schlittler, L.; Smakal, M.; Stahalova, V.; Sternberg, C.; Seufferlein, T.; Tebbutt, N.; Vinholes, J. J.; Wadlow, R.; Wenczl, M.; Wong, M. Nanoliposomal irinote-

can with fluorouracil and folinic acid in metastatic pancreatic cancer after previous gemcitabine-based therapy (NAPOLI-1): a global, randomised, open-label, phase 3 trial. *The Lancet* **2016**, *387*, 545–557.

(30) Armstrong, J.; Wenby, R.; Meiselman, H.; Fisher, T. The Hydrodynamic Radii of Macromolecules and Their Effect on Red Blood Cell Aggregation. *Biophysical Journal* **2004**, *87*, 4259–4270.

(31) Li, Y.; Qiao, Y.; Chen, H.; Bai, R.; Staedtke, V.; Han, Z.; Xu, J.; Chan, K. W.; Yadav, N.; Bulte, J. W.; Zhou, S.; van Zijl, P. C.; Liu, G. Characterization of tumor vascular permeability using natural dextrans and CEST MRI. *Magnetic Resonance in Medicine* **2018**, *79*, 1001–1009.

(32) Cabral, H.; Matsumoto, Y.; Mizuno, K.; Chen, Q.; Murakami, M.; Kimura, M.; Terada, Y.; Kano, M.; Miyazono, K.; Uesaka, M.; Nishiyama, N.; Kataoka, K. Accumulation of sub-100 nm polymeric micelles in poorly permeable tumours depends on size. *Nature Nanotechnology* **2011**, *6*, 815.